Stability Investigation of High Enthalpy Boundary Layer Flow with Gas Injection using Energy Budget Analysis

Vincenzo Russo *1, Bijaylakshmi Saikia †1, and Christoph Brehm ‡1

1 Department of Aerospace Engineering, University of Maryland, College Park, MD 20742, USA

The management of intense thermal loads encountered by hypersonic vehicles operating in the atmosphere can be effectively alleviated by utilizing transpiration cooling, which involves the injection of cold fluids at the vehicle's surface. However, this injection process can substantially impact flow stability and potentially induce a premature transition to turbulence. The primary objective of this study is to comprehensively understand the mechanisms responsible for destabilizing flow during transpiration cooling application. To assess the influence of injection gas properties on the stability of high-enthalpy boundary layer flows, air and CO_2 injections are being considered. Both fluids are introduced at the same mass flux, resulting in a comparable reduction in heat flux. A reduction in the boundary layer thickness was noted due to the decrease in thermal-diffusivity with CO_2 injection compared to air. The injection of air caused the neutral curve to shift further upstream compared to the no-blowing case. Additionally, the frequency leading to the maximum amplification shifted to lower values due to increased Reynolds number based on the boundary layer thickness. The increased destabilization observed with CO_2 injection can be attributed to reduced dissipation compared to air injection.

I. Introduction

High-speed vehicles operating in the atmosphere are subject to severe thermal loads. Several strategies for thermal management exist that can be employed to mitigate the high thermal loads. This study focuses on the application of transpiration cooling techniques, which aim to reduce heat flux by introducing a cold transpiration gas through the wall to displace the high-temperature boundary layer flow. Typically, the transpiration fluid is injected tangentially (film cooling) or orthogonal through the wall through a porous surface (transpiration cooling). Additional reduction of heat transfer rates is expected when adopting inert compounds, which prevents recombination close to the wall. While the cooling effectiveness for different transpiration fluids has been investigated by various researchers [1–11] the effects on boundary layer transition are not fully understood, especially in high-temperature boundary layer regime where "real gas" effects are relevant.

In early investigations, Pappas *et al.* [12] and Marvin *et al.* [13] conducted experiments aimed at measuring wall heat flux and examining the impact of blowing on boundary layer transition. These experiments encompassed a spectrum of Mach numbers, utilizing thermocouples to ascertain transition locations. The findings indicated that premature transition can be induced by outgassing. Notably, the atomic/molecular weight of the injected compound emerged as a significant factor influencing the transition process. Specifically, lighter gases were found to promote transition, while heavier ones demonstrated a stabilizing effect. This observation has been corroborated by several recent experimental inquiries [14–16].

Several numerical research studies have delved into investigating the stability mechanisms associated with wall blowing, utilizing Linear Stability Theory (LST) as a key tool [17, 18]. Mortensen *et al.* [19] incorporated a real gas formulation that factors in thermo-chemical non-equilibrium and ablation effects. Consistent with experimental findings, these numerical studies confirmed the destabilizing effect of wall injection. It is pertinent to note that wall injection can significantly alter the baseflow, making non-parallel effects more relevant, thus introducing inaccuracies in growth rate predictions when employing the parallel flow assumption in LST. Li *et al.* [20], utilizing Direct Numerical Simulation (DNS) and LST, somewhat surprisingly discovered that strong outgassing led to a weak stabilization in a second mode dominated transitional flow on a slender cone. This observation was further substantiated for a high Mach number flat plate boundary layer flow. In a recent investigation, Saikia *et al.* [21] reported a notable destabilizing effect resulting

^{*}Graduate Research Assistant and AIAA member.

[†]Postdoctoral Researcher and AIAA Member.

[‡]Associate Professor and AIAA Member.

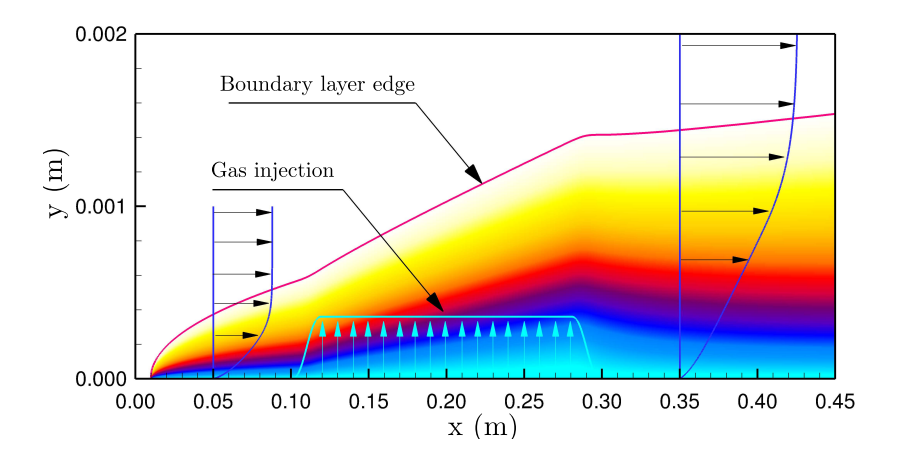


Fig. 1 Simulation setup for the injection cases with color contours of streamwise velocity. The velocity and injection profiles are extracted from the air injection case with a velocity of 0.3 m/s.

from gas injection on a blunt cone. Their findings revealed a direct correlation between injection velocity and the location of transition onset, suggesting a linear relationship.

The influence of various injection gases on the transition process has been reexamined by Miró Miró et al. [22], shedding new light on the findings from experimental campaigns conducted in the late 1960s and 1970s. Miró Miró et al. demonstrated that the stability of the boundary layer is not solely determined by the atomic or molecular weight of the injection gas. Instead, it is significantly influenced by a range of additional parameters such as injection patterns/profiles and wall porosity. The injection of gases such as CO₂ may also serve to delay the transition by absorbing acoustic energy within an enthalpy range relevant to high-temperature applications [15, 23, 24].

Previous research [25] has established that the injector geometry and injection pattern can exert a substantial influence on the N-factor envelopes. This current study primarily aims to explore the impact of injection gas properties on the transition process, specifically by comparing the effects of air and CO₂ injection. To facilitate this investigation, a basic flat plate boundary layer flow with a smoothed top hat injection profile at the wall is selected. The illustration in Figure 1 depicts the simulation setup in our current research, with wall injection applied at a specific streamwise window. The color contours of the streamwise velocity are utilized to delineate the boundary layer region, where an increase in boundary layer thickness is observed along the injection slot. This augmentation in boundary layer thickness leads to a shift of the most unstable frequencies towards lower values, as evidenced in prior studies such as Refs. 21 and 25. Moreover, apart from frequency shift, other attributes of the instability mode are also influenced. Notably, previous works [21] revealed that injection of a cold fluid decelerates the phase speeds of instability modes, thereby promoting the emergence of the supersonic mode [26]. A spatial energy budget analysis will be used to comprehend how the gas properties of the injected fluid affect the transition process.

The article is structured as follows: Section II outlines the governing equations, Section III provides an in-depth analysis of the baseflow results, Section IV presents the findings of the disturbance calculations, and Section V encompasses the energy budget analyses. Finally, conclusions are derived in Section VI.

II. Governing Equations

To model thermo-chemical non-equilibrium flow (TCNE), we utilize an 8-species air-carbon reaction model encompassing N_2 , N_2 , N_2 , N_3 , N_4 , N_4 , N_5 , N_5 , N_5 , N_5 , N_6 , $N_$

$$N_2 + M \rightleftharpoons N + N + M$$

$$O_2 + M \rightleftharpoons O + O + M$$

 $NO + M \rightleftharpoons N + O + M$
 $CO_2 + M \rightleftharpoons CO + O + M$
 $CO + M \rightleftharpoons C + O + M$.

Here, M denotes the collision partner. The exchange reactions can be written as,

$$NO + O \rightleftharpoons O_2 + N$$

$$N_2 + O \rightleftharpoons NO + N$$

$$CO + O \rightleftharpoons C + O_2$$

$$CO_2 + O \rightleftharpoons O_2 + CO$$

$$CO + N \rightleftharpoons NO + C$$

$$CO + CO \rightleftharpoons CO_2 + CO$$

$$CO + NO \rightleftharpoons CO_2 + N$$

$$N_2 + O_2 \rightleftharpoons NO + NO.$$

The Navier-Stokes equations corresponding to thermo-chemical non-equilibrium flow are given by:

$$\frac{\partial U}{\partial t} + \nabla \cdot \left(F_c - F_v \right) + \frac{1}{y} (H_c - H_v) = W, \tag{1}$$

where $U = \{\rho_1, \dots, \rho_{ns}, \rho u, \rho v, \rho w, E, E_v\}^T$ represents the conservative state vector, with ρ_s and ρ denoting the species and total fluid density, respectively. The convective flux F_c and the viscous flux F_v can be expressed as:

$$F_{c} = \begin{cases} \rho_{1}\hat{u} \\ \vdots \\ \rho_{ns}\hat{u} \\ \rho u\hat{u} + p\delta_{1i} \\ \rho v\hat{u} + p\delta_{2i} \\ \rho w\hat{u} + p\delta_{3i} \\ (E+p)\hat{u} \\ E_{v}\hat{u} \end{cases} \text{ and } F_{v} = \begin{cases} -J_{1} \\ \vdots \\ -J_{ns} \\ \tau_{1i} \\ \tau_{2i} \\ \tau_{3i} \\ q_{tr} + q_{ve} - \sum_{s=1}^{ns} J_{s}h_{s} + \tau \cdot V \\ q_{v} - \sum_{s=1}^{ns} J_{s}e_{v,s} \end{cases} . \tag{2}$$

The fluid velocity vector U is represented by $\{u, v, w\}^T$ in the Cartesian reference frame. The total energy and vibrational energy per unit volume are denoted by E and E_v , respectively. The contravariant velocity is denoted by \hat{u} , mixture pressure by p, and viscous stress tensor by τ . The mass-diffusion flux and species enthalpy are denoted by J_s and h_s , respectively. The heat flux components for the translational/rotational modes q_{tr} and vibrational energy modes q_{ve} are evaluated using the Fourier's law of heat conduction. To compute the mixture viscosity and conductivity, the Wilkes mixing rule [28] is utilized, while species viscosity and conductivity are determined using the curve fits of Blottner et al. [29] and Eucken's relation [30]. The term W in Eq. (1) represents the thermo-chemical non-equilibrium source term.

$$\mathbf{W} = \left\{ \omega_1 \quad \cdots \quad \omega_{ns} \quad 0 \quad 0 \quad 0 \quad 0 \quad S_{t2v} + S_{c2v} \right\}^T, \tag{3}$$

where ω_s represents the net chemical production rate for each species s. To account for energy exchange from translational to vibrational modes, we use the source term S_{t2v} . On the other hand, vibrational to chemical energy exchange is achieved through the use of S_{c2v} . Finally, the chemical source terms for each species are written as follows.

$$\omega_s = M_s \sum_{1}^{nr} \dot{w}_{sr},\tag{4}$$

where \dot{w}_{sr} is the chemical production rate of species s in reaction r and is given by

$$\dot{w}_{sr} = (v_{sr}^{"} - v_{sr}^{'}) \left[k_{fr} \prod_{j=1}^{ns} \left(\frac{\rho_j}{M_j} \right)^{\nu_{jr}^{'}} - k_{br} \prod_{j=1}^{ns} \left(\frac{\rho_j}{M_j} \right)^{\nu_{jr}^{"}} \right]. \tag{5}$$

For a given reaction r, v' and v'' are the stoichiometric coefficients for the reactants and the products, respectively. The terms k_{fr} and k_{br} represent the forward and backward reaction rates, with nr denoting the total number of reactions. Additional details about how the transport quantities are computed, species energy state and transport data and Arrhenius curve fit coefficients are provided in Appendix A, B, and C, respectively. The TCNE baseflow solver has been validated in various prior research efforts [31–33].

Upon achieving the steady converged mean flow, the linear disturbance equations (LDE) for a perfect gas flow are derived by subtracting the mean flow from the instantaneous equations and disregarding the non-linear terms in the disturbances. This can be expressed as:

$$\frac{\partial \tilde{\mathbf{U}}}{\partial \tilde{\mathbf{Q}}} \frac{\partial \tilde{\mathbf{Q}}}{\partial t} + \frac{\partial \tilde{\mathbf{F}}_{\mathbf{i}}}{\partial x_i} + \frac{\partial \tilde{\mathbf{F}}_{\mathbf{v}_i}}{\partial x_i} = \mathbf{0}; \tag{6}$$

Here, the primitive state vector $\tilde{\mathbf{Q}}$, denoting the disturbance quantities, is defined as $[\tilde{p}, \tilde{u}, \tilde{v}, \tilde{T}]'$. $\partial \tilde{\mathbf{U}}/\partial \tilde{\mathbf{Q}}$ is the transformation matrix from conservative to primitive state vector. The conservative vector for disturbances along with the fluxes $\tilde{\mathbf{F}}$ and $\tilde{\mathbf{F}}_{v}$ can be written as

$$\tilde{\mathbf{U}} = \begin{bmatrix} \tilde{\rho} \\ \tilde{\rho}\bar{u} + \bar{\rho}\tilde{u} \\ \tilde{\rho}\bar{v} + \bar{\rho}\tilde{v} \\ \tilde{E} \end{bmatrix}; \quad \tilde{\mathbf{F}} = \begin{bmatrix} \tilde{\rho}\bar{u} + \bar{\rho}\tilde{u} \\ \bar{\rho}\bar{u}\tilde{u}_{i} + \bar{\rho}\bar{u}_{i}\tilde{u} + \tilde{\rho}\bar{u}_{i}\tilde{u} + \tilde{\rho}\tilde{u}_{i}\tilde{u} \\ \bar{\rho}\bar{v}\tilde{u}_{i} + \bar{\rho}\bar{u}_{i}\tilde{v} + \tilde{\rho}\bar{v}\bar{u}_{i} + \tilde{P}\delta_{2i} \\ (\bar{E} + \bar{P})\tilde{u}_{i} + (\tilde{E} + \tilde{P})\tilde{u}_{i} \end{bmatrix}; \quad \tilde{\mathbf{F}}_{\mathbf{v}} = \begin{bmatrix} 0 \\ -\tilde{\tau}_{1i} \\ -\tilde{\tau}_{2i} \\ -\tilde{\kappa}\frac{\partial \tilde{T}}{\partial x_{i}} - \tilde{\kappa}\frac{\partial \tilde{T}}{\partial x_{i}} - \tilde{\tau}_{ij}\tilde{u}_{j} - \bar{\tau}_{ij}\tilde{u}_{j} \end{bmatrix}.$$

An overbar denotes the mean flow terms, and δ_{ij} represents the Kronecker delta function. In terms of specific heat at constant volume C_{ν} and specific gas constant R, the total energy of the disturbance can be written as

$$\tilde{E} = \bar{\rho}C_{v}\tilde{T} + \tilde{\rho}C_{v}\bar{T} + \bar{\rho}\bar{u}\tilde{u} + \bar{\rho}\bar{v}\tilde{v} + 0.5\tilde{\rho}(\bar{u}^{2} + \bar{v}^{2}).$$

The equations used to calculate the disturbance flow field are based on the assumption of a perfect gas. The mean flow, however, along with the transport and gas properties utilized in these calculations, are derived from the TCNE simulation. The mean flow properties include mixture pressure, velocity, and translational temperature, while transport properties encompass mixture viscosity and conductivity. Furthermore, the TCNE solver is utilized to provide derivative information for the computation of disturbance viscosity ($\tilde{\mu} = \frac{d\tilde{\mu}}{dT}\tilde{T}$) and thermal conductivity ($\tilde{\kappa} = \frac{d\tilde{\kappa}}{dT}\tilde{T}$). Gas properties such as specific gas constant, ratio of specific heat, specific heat at constant pressure, and speed of sound are also calculated based on the TCNE simulation results.

The convective terms are discretized using a fifth-order Weighted Essentially Non-Oscillatory (WENO) scheme [34, 35] in conjunction with a Rusanov flux vector splitting method. Meanwhile, the viscous terms are discretized based on a second-order central scheme. The mean flow computation involves a first-order backward-difference scheme to advance the governing equations in pseudo-time until reaching a steady state. Furthermore, to optimize computational costs, a time-spectral solver [36, 37] is utilized for evolving the linear disturbance equations over time. This solver employs a direct solution approach with two collocation points or time samples to determine the periodic steady state during the linear stage of flow transition to turbulence. When discretizing the time-derivative term in Eq. (6), a spectral differentiation operator \mathbf{D}_N is employed — representing the steady state residual $\tilde{\mathbf{R}}$ and the disturbance forcing term as $\tilde{\mathbf{S}}$ enables the direct inversion of the system of equations that govern the linear disturbance equation:

$$\left(\frac{\partial \tilde{\mathbf{U}}}{\partial \tilde{\mathbf{Q}}} \mathbf{D}_{N} - \frac{\partial \tilde{\mathbf{R}}}{\partial \tilde{\mathbf{Q}}}\right|_{\mathbf{min}}\right) \tilde{\mathbf{Q}} = \tilde{\mathbf{S}}.$$
 (7)

In the aforementioned expression, numerical Jacobians are utilized to approximate the exact Jacobian matrix of the residual $\tilde{\mathbf{R}}$. The PETSc (Portable, Extensible Toolkit for Scientific Computation) library [38] is employed, along with linear direct solvers from the external package MUMPS (MUltifrontal Massively Parallel sparse direct Solver) [39], for the direct inversion of Eq. (7) under the assumption of infinite local CFL (Courant–Friedrichs–Lewy number). In the case of the time spectral solver, a continuous volume forcing is utilized to introduce disturbances through the wall. This can be expressed as,

$$S(x, y, t) = A \sin\left(\frac{2\pi(x - x_o)}{\Delta x_w}\right) \exp\left(-\frac{(y - y_o)^2}{\sigma_y}\right) \cos(\omega t), \tag{8}$$

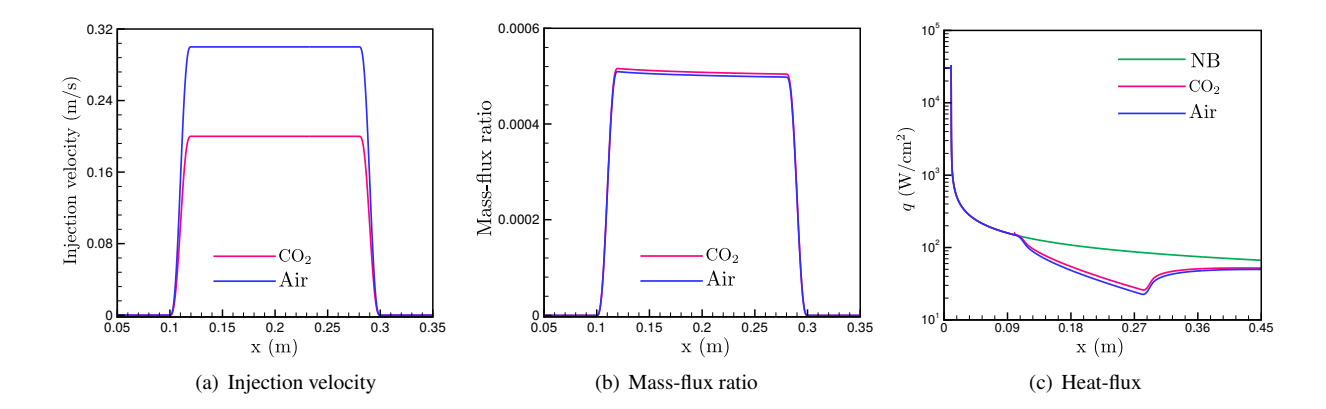


Fig. 2 The distribution of (a) injection velocity, (b) mass-flux ratio, and (c) heat-flux plotted along the wall for the no-blowing, air injection and CO₂ injection cases.

At a specified circular frequency ω , the disturbance is introduced at (x_o, y_o) to analyze the stability characteristics of the flow field. The parameter σ_y governs the pulse width in the wall-normal direction, while Δx_w represents the width of the forcing slot.

III. Simulation of the Mean Flow Field

The experimental conditions for this study correspond to the tests conducted at the GALCIT Free-Piston Shock Tunnel, T5, located at the California Institute of Technology, utilizing a sharp cone geometry. Here, a flat plate geometry was employed at a Mach number of 4.35. The translational and vibrational temperatures in the freestream were recorded at 1884 K and 1445 K, respectively, alongside a flow pressure of 46.132 kPa. These represent post-shock conditions downstream of the nose of a blunt cone with a radius of 5.08. Simulation conditions for the blunt cone were selected to replicate the 2541 shot at the T5 tunnel, where the free stream temperature and pressure were 1369.4 K and 21.89 kPa respectively [24]. The Mach number and stagnation enthalpy of the flow were noted as 5.3 and 9.51 MJ/kg, while the surface temperature was maintained at 293 K.

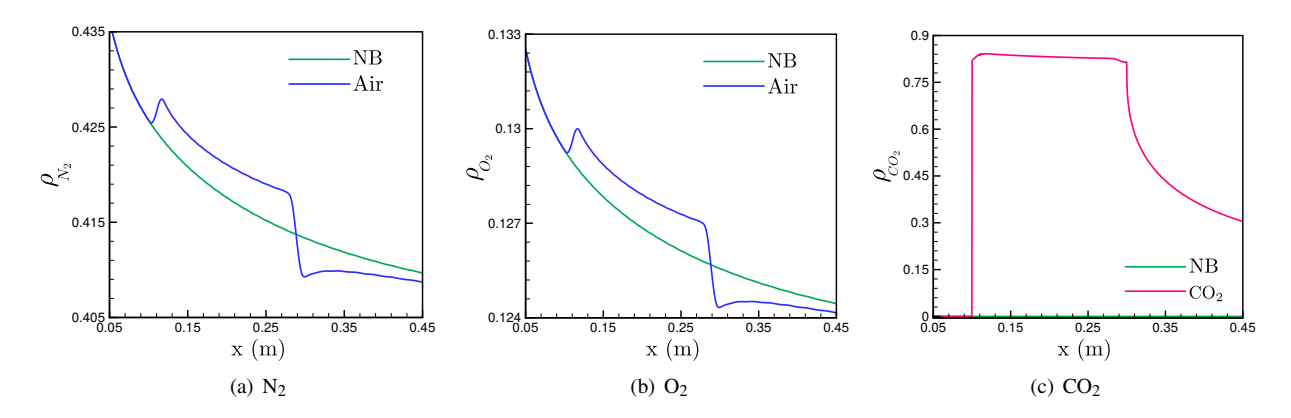


Fig. 3 The variation of density along the wall for (a) N_2 and (b) O_2 with air injection compared with the no-blowing case. The density of CO_2 is shown in (c) generated due to the injection of this gas.

The wall enforces no-slip and no-penetration boundary conditions, except at the injection slot. Additionally, non-catalytic boundary conditions were used to maintain zero mass-fraction gradients at the wall. The computational grid comprised 6000 grid points in the streamwise direction and 300 in the wall-normal direction. The grid points were concentrated near the wall and stretched further away. Before selecting this grid with a wall-normal spacing of $dy_w = 10^{-6}$ m, a thorough grid convergence study was conducted. The heat flux variation as a function of dy_w is reported in Appendix E.

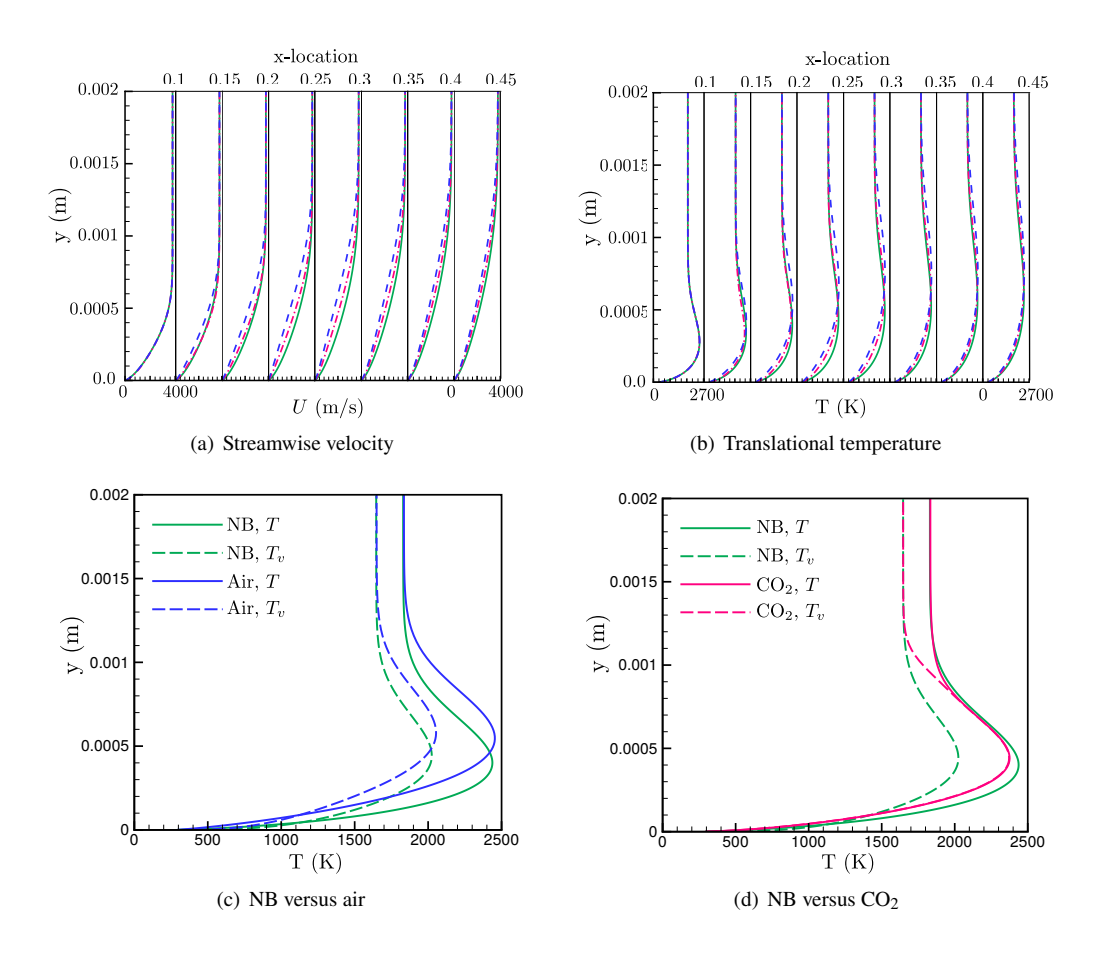


Fig. 4 The variation of (a) streamwise velocity and (b) translational temperature compared between no-blowing, air and \mathbf{CO}_2 injection cases at different locations above the flat plate. A comparison of translational and vibrational temperatures at x = 0.2 m is shown in the bottom panel.

Table 1 outlines the various cases examined in this transpiration cooling study. Case I represents the non-blowing scenario (NB). In subsequent cases, injection is applied between x = 0.1 m and 0.3 m. For case II, air is introduced with a composition corresponding to the free-stream mass fraction. Conversely, case III injects a gas consisting entirely of CO_2 with a mass fraction of 1.0. To maintain a consistent mass-flux between air and CO_2 injection, both gases were injected at different velocities. The distribution of injection velocity and mass-flux ratio is shown in Figures 2(a) and 2(b), respectively. The effect of injection velocity on the wall-heat flux is shown in Figure 2(c). A reduction in heat flux values with air and CO_2 injection in comparison to the no-blowing case is noted. Although there is a 50% reduction in translational conductivity with CO_2 injection as compared to air, there is a similar increase of translational temperature gradient, which leads to similar heat-flux values between air and CO_2 injections.

Cases	Injection gas composition	Blowing velocity (m/s)
I	NB	0
II	$N_2 = 0.767, O_2 = 0.233$	0.3
III	$CO_2 = 1.0$	0.2

Table 1 Transpiration cooling cases considered in this work where the injection is applied between 0.1 - 0.3 m.

Figures 3(a) and 3(b) illustrate the variation of species density for N_2 and O_2 along the wall, in the case of air injection. The variation of CO_2 generated due to the injection of this gas with a mass-fraction of 1 is shown in Figure 3(c).

In both scenarios, there is a noticeable increase in the densities of the injected species from the outgassing onset location. Although the increase in wall density for the air case is minimal, the density of CO_2 is significantly higher.

The variations in streamwise velocity and temperature profiles resulting from the outgassing through the wall are depicted in Figures 4(a) and 4(b), respectively. The boundary layer profile associated with the injection of CO_2 undergoes a sudden thinning in close proximity to the injection onset location (x = 0.1 m), attributed to rapid alterations in thermal diffusivity. This phenomenon has been previously highlighted in the work of Miró Miró et al. [22].

Further downstream, the velocity profiles show a progressive thickening. More specifically, it can be observed that the boundary layer is thicker when air is injected. This trend is expected due to the higher injection velocity required for air outgassing to preserve the same mass flux ratio. A comparison of translational and vibrational temperatures between the no-blowing case and air injection case is depicted in Figure 4(c), while CO_2 is contrasted with the no-blowing case in Figure 4(d). The temperature profiles exhibit similar trends to the velocity profiles, with peak temperatures being pushed away from the wall due to gas injection. In contrast to the presence of strong thermal non-equilibrium within the boundary layer in the no-blowing and air injection case, the injection of CO_2 establishes a region of thermal equilibrium flow near the wall.

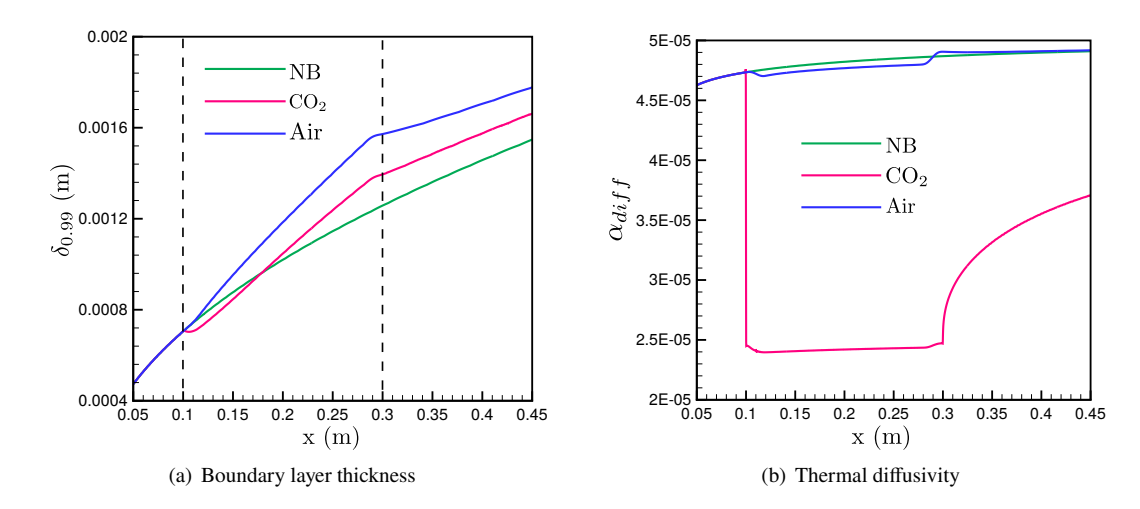


Fig. 5 A comparison of (a) boundary layer thickness and (b) thermal diffusivity along the wall are shown for the no-blowing, air injection, and CO₂ injection cases.

The increased boundary layer thickness resulting from air injection, as depicted in Figure 5(a), is anticipated to lead to the destabilization of the second mode and a subsequent reduction in its characteristic frequency [17, 18, 40]. In the case of CO₂, the initial kink and subsequent decrease in boundary layer thickness are attributed to changes in the gas and thermodynamic properties. Gas injection generally influences boundary layer thickness in two ways: 1) by introducing mass into the boundary layer, thereby causing a displacement effect, and 2) by altering gas properties that impact mass, momentum, and energy diffusion. When gas with very low thermal diffusivity is injected at the wall, the diffusion-based mechanisms of mass, momentum, and heat transfer become less effective, leading to a reduction in boundary layer thickness. Conversely, higher diffusivity induces the opposite effect. Figure 5(b) illustrates the diffusivity at the wall for air and CO₂ injection cases, revealing a significant reduction in thermal diffusivity for the CO₂ case.

IV. Simulation of Disturbance Flow-field

The disturbance flow field is computed considering the thermo-chemical non-equilibrium mean flow in conjunction with the computed gas and transport properties. The time-spectral solver is utilized to simulate the disturbance flow field by applying continuous wall momentum forcing through a slot at the wall at a specified frequency. Figure 6 presents a comparison of the results from wall-forcing (WF) with the data acquired from introducing fast acoustic waves (FA) in the free stream upstream of the leading edge of the flat plate boundary layer.

The receptivity process is expected to differ between the two approaches; however, both result in a similar variation of wall-pressure amplitude for the no-blowing case as depicted in Figure 6(a) at 1500 kHz. Upon completion of the

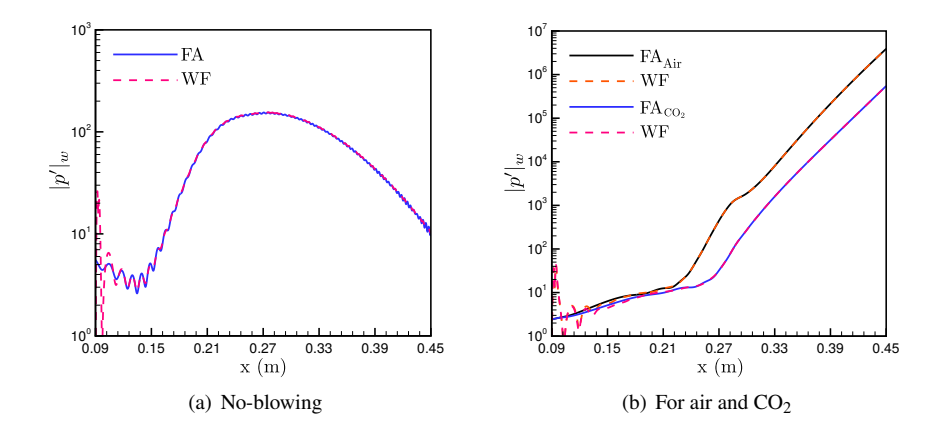


Fig. 6 A comparison of wall-pressure amplitudes obtained after free-stream forcing versus wall-forcing for (a) the no-blowing case at 1500 kHz and (b) air and CO₂ injection cases at 700 kHz.

receptivity phase, a similar pattern is observed in the context of both air and CO_2 injection, computed at a frequency of 700 kHz, as shown in Figure 6(b). Consequently, in the subsequent discussions in this paper, we will exclusively present the findings derived from computations involving the wall-forcing of disturbances.

To illustrate the effect of gas injection on the disturbance flow field, disturbance wall-pressure amplitude was computed, and it is plotted in Figure 7. A comparison between the air injection case and the no-blowing case reveals that injecting air at a velocity of 0.3 m/s results in nearly three orders of magnitude increase in the wall-pressure amplitude at the end of the domain but in a very narrow range of frequencies.

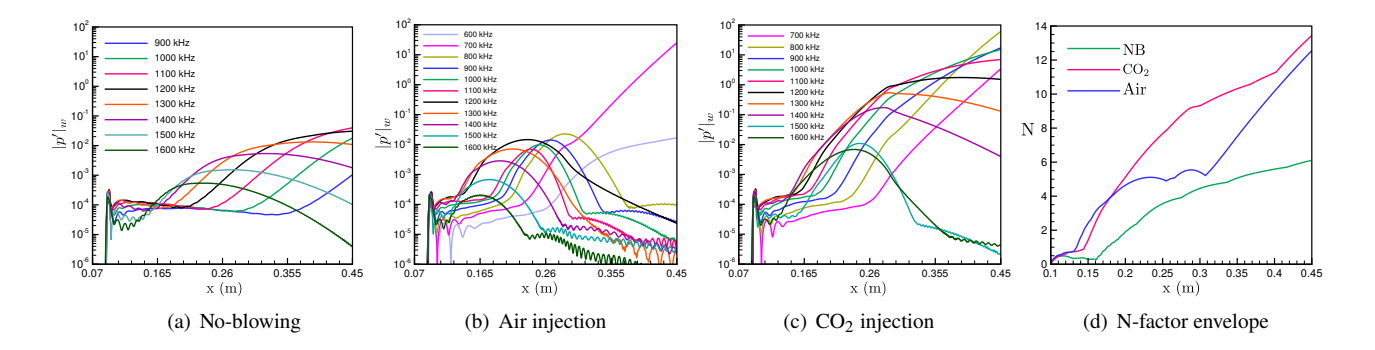


Fig. 7 The variation of wall-pressure amplitude for a range of frequencies compared between the (a) no-blowing, (b) air injection, and (c) CO₂ injection case. A comparison of the N-factor envelope for three cases is shown in (d).

The injection of air leads to an increase in the boundary layer thickness, causing a shift in the frequency of the most amplified mode from 1100 kHz to 700 kHz for the amplitude curve, reaching the largest amplitude at the end of the computational domain. In contrast to the no-blowing case, where disturbance growth is observed almost throughout the domain, air injection causes enhanced amplification downstream of the injection location (x > 0.1m), particularly at higher frequencies (refer to Figures 7(a) and 7(b)). A reduction in the receptivity region is also noted due to gas injection. The introduction of CO_2 alters the gas properties, leading to a distinctly different disturbance pressure variation compared to air injection across the considered frequency range. The wall-pressure amplitude exhibits the largest increase at 800 kHz (at the end of the computational domain) as a consequence of the reduced boundary layer thickness resulting from CO_2 injection as compared to air injection. However, as illustrated in Figure 7(c), an enhanced amplification of disturbances is evident across a broad frequency range throughout the domain when CO_2 is injected.

The variation of the N-factor envelope for the three cases is displayed in Figure 7(d). Both air and CO₂ injection result in a larger N-factor envelope than the no-blowing case. While air injection initially slightly exceeds the N-factor of the CO₂ case, it exhibits a sudden decline before rising again towards the end of the injection location. Ultimately,

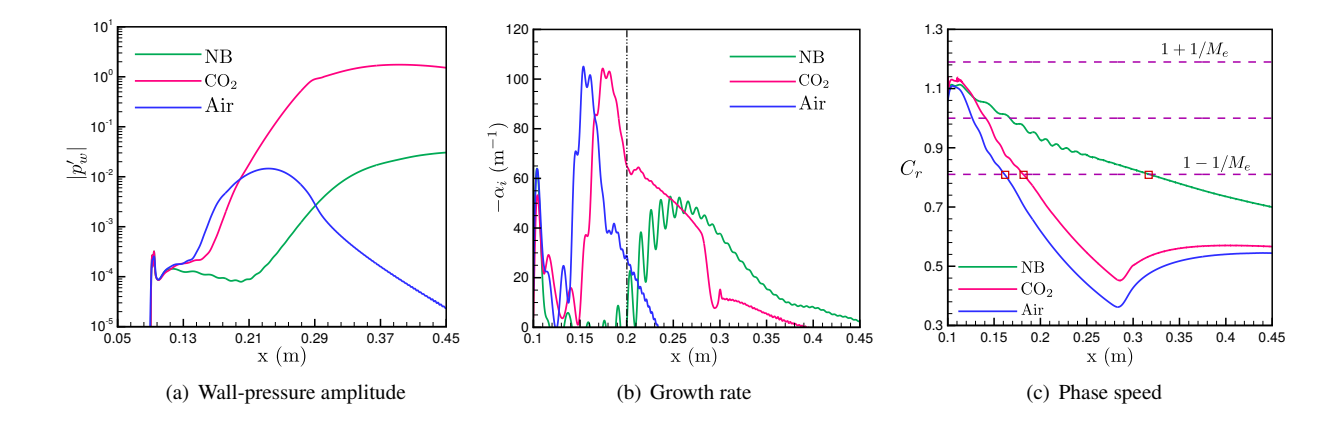


Fig. 8 Comparison of (a) wall-pressure, (b) growth rate and (c) phase speed between the no-blowing, CO₂, and air injection case at 1200 kHz. The onset of the supersonic mode is marked by the small red square in (c).

comparable N-factor values are observed for both air and CO_2 injection at the end of the domain. If the transition N-factor is assumed to be 9, it can be inferred that CO_2 will cause an earlier transition than air injection, causing the transition to occur at x = 0.28 m instead of x = 0.38 m for air. To comprehend the physical mechanisms contributing to the destabilization of the flow resulting from gas injection, a comprehensive energy analysis is conducted in the subsequent section.

V. Analysis of the Disturbance Flow-field using Energy Budget

For the energy budget analysis, 1200 kHz has been selected, for which CO_2 exhibits a much larger wall-pressure amplitude compared to air injection, as can observed in Figure 8(a). However, both air and carbon dioxide injections show similar peak amplification rates. The primary distinction between the two cases is that the x-location corresponding to the peak growth rate for air injection is slightly ahead of the CO_2 location, which is caused by an increased Re_δ . Furthermore, CO_2 injection results in the unstable region extending until $x \approx 0.4$ m, whereas air injection leads to a much smaller unstable region extending until x = 0.23 m. In the absence of blowing, the amplification of disturbances is only observed after reaching a distance of x = 0.2 m. However, the peak amplification rate is notably reduced, and the disturbances continue to become unstable throughout the rest of the domain.

To identify the dominant instability modes present in the flow field, we computed the phase speed along the wall using the disturbance pressure. The dashed-dotted lines labelled as $1 + 1/M_e$ and $1 - 1/M_e$ in Figure 8(c) correspond to the phase speed of the continuous fast acoustic and slow acoustic waves, respectively, with an edge Mach number of M_e . The vorticity and entropy waves travel with a velocity of $c_r = 1$. In all cases depicted in the figure, the receptivity process results in a mode with a phase similar to the fast acoustic waves, referred to as the fast mode F_1^+ [41]. This mode synchronizes with the vorticity/entropy waves downstream of the injection location for air and CO₂ cases. Proceeding along the flat plate, we witness the emergence of the second mode in the flow $(1-1/M_e < c_r < 1)$, which transitions into the supersonic mode upon reaching a phase speed comparable to that of the slow acoustic waves. For the no-blowing case, the supersonic mode manifests in the flow at x = 0.32 m, denoted by the small red square. Introducing CO₂ at a velocity of 0.2 m/s induces an upstream shift of the supersonic mode, leading to its appearance at approximately x = 0.18 m. Meanwhile, air injection at 0.3 m/s propels this mode even further upstream along the flat plate. This can also be verified by comparing the flow fields between air and CO₂ injection presented in Figures 9(c) and 9(d), respectively in terms of the real component of the disturbance pressure contours. For the no-blowing case, the first mode remains the dominant instability mode until approximately x = 0.3 m, as highlighted in Figure 9(a). Beyond this point, Mack's second mode transiently emerges before evolving into the supersonic mode, as shown in Figure 9(b) at 1200 kHz.

As outlined in Appendix D, Chu's energy norm [42], also known as "Mack norm" due to its extensive use in Mack's report [43], is used to perform energy budget analysis in this work. Notably, Chu's energy norm, originally devised for perturbations within temporal stability analysis, has been adapted for analyzing spatially growing perturbations in

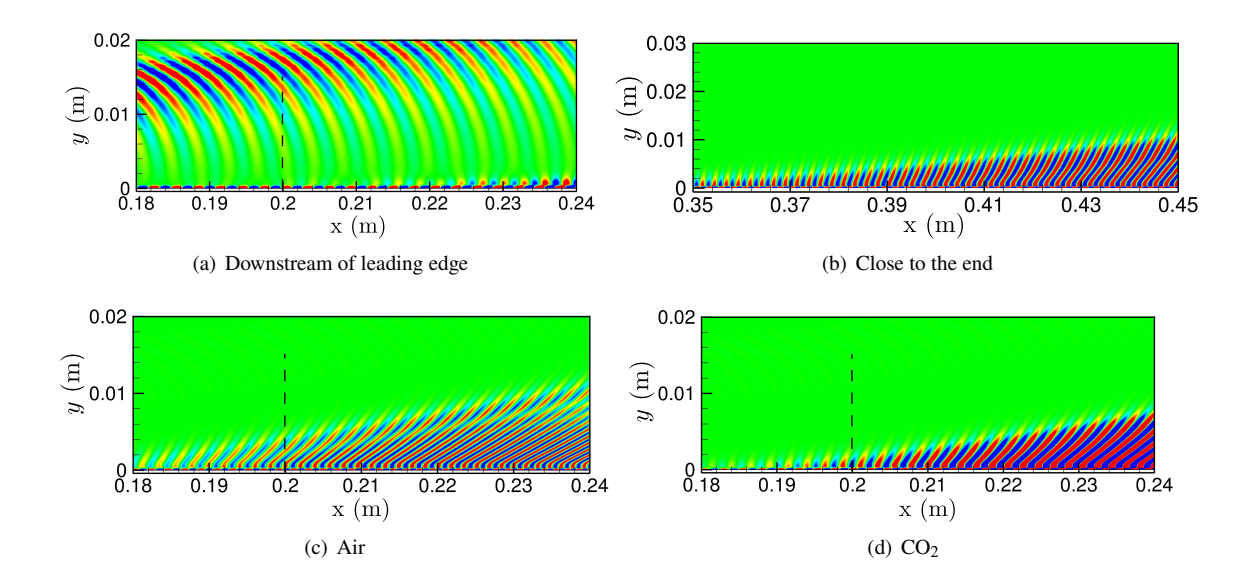


Fig. 9 The disturbance flow field is shown in terms of pressure contours for the no-blowing case at the top panel at 1200 kHz. Air and CO₂ injection cases are shown at the bottom panel at the same frequency.

this study despite a lack of explicit justification for this adaptation [44]. Therefore, the validity of the budget analysis approach is first assessed in Figure 10. Appendix D provides the precise formulations for these additional terms manifest when formulating energy budgets based on Mack's energy norm. Since we use the budget analysis to explain the differences in the disturbance amplification, they are computed as contributions to the spatial growth rate. In evaluating all scenarios, specifically, those involving no blowing, air injection, and CO₂ injection, it is evident that these terms exhibit relatively minimal magnitudes when contrasted with the predominant terms depicted in Figure 11.

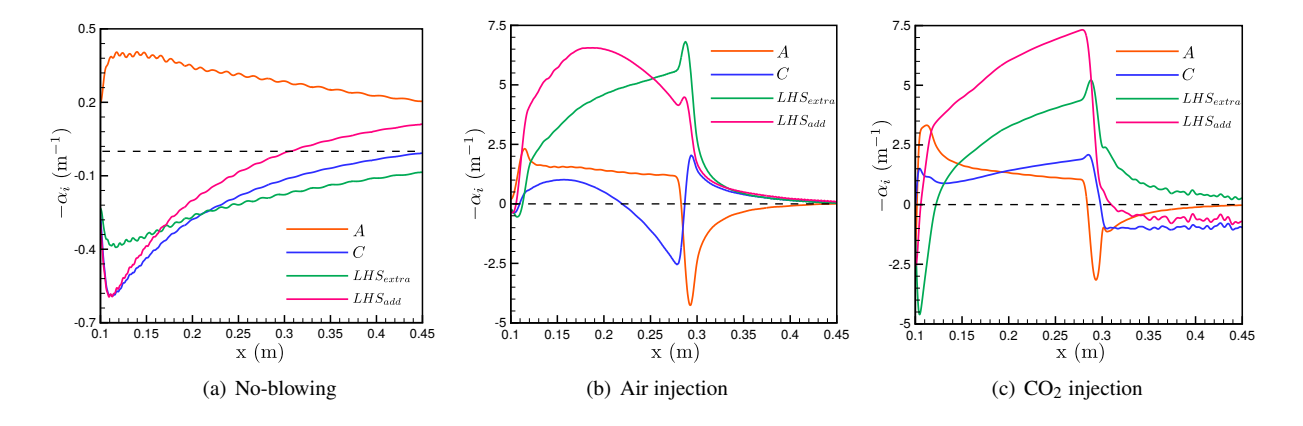


Fig. 10 The additional terms in the RHS of the energy budget equation is shown for the (a) no-blowing, (b) air injection and (c) CO₂ injection case at 1200 kHz.

However, it is important to note that the impact of these additional terms increases significantly upon the application of injection, with a discernible order of magnitude growth becoming evident.

Upon establishing the validity of the budget analysis approach, we provide an overview of the different energy transfer mechanisms in Figure 11 after integrating along the boundary layer. For the no-blowing case, the dominant production term is P_{TP} , which appears due to the variation of transport properties. However, the destabilization of the instability mode at 1200 kHz appears to be related to an increase in the Reynolds stress term P_{RS} as can be seen from Figure 11(a). Among the dissipation terms, the heat flux generated through conduction provides the most significant

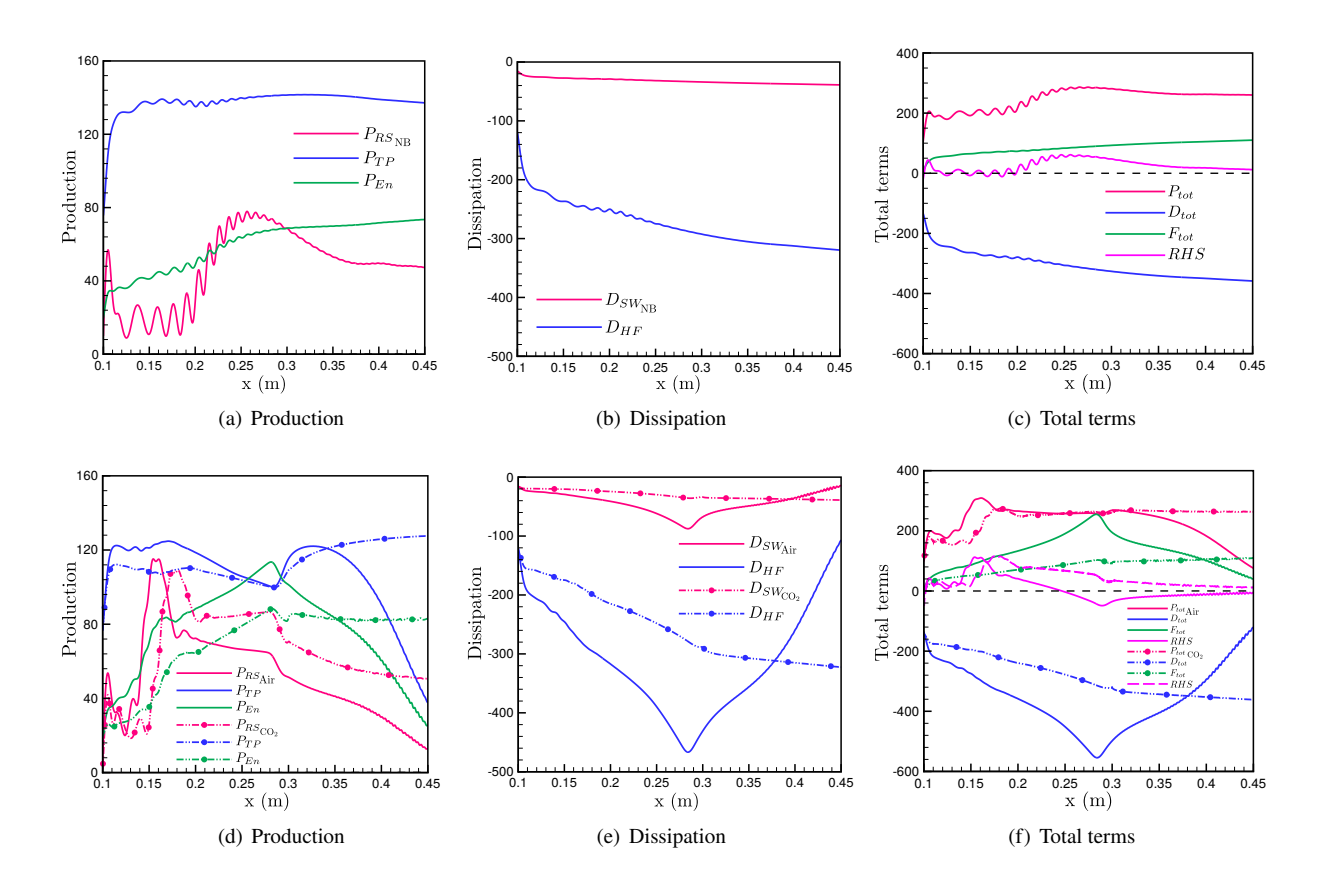


Fig. 11 The top panel shows the growth rates computed based on the dominant energy transfer terms integrated along the wall-normal direction for the no-blowing case. Air and \mathbf{CO}_2 cases are compared at the bottom panel at 1200~kHz.

energy reduction, as seen from the variation of D_{HF} along the flat plate in Figure 11(b). A comparative analysis of the total energy transfer constituents illustrated in Figure 11(c) reveals that the rate of change of total disturbance energy closely tracks the variation of the total production term, albeit with a reduced magnitude due to the balance among different energy transfer mechanisms.

The main objective is to understand the different stability mechanisms for the two injection scenarios by comparing the dominant constituents of various production and dissipation terms in Figure 11(d) and 11(e), respectively. For both air and CO_2 , the dominant production term remains to be P_{TP} , consistent with that of the no-blowing case. Despite not being the predominant factor, the heightened P_{RS} appears to instigate flow destabilization. Beyond the peak amplification location at approximately x = 0.15 m, it is noteworthy that the Reynolds stress term exhibits a significantly greater magnitude in the case of CO_2 . When the second mode transitions into a supersonic mode, the entropy term P_{En} term emerges as the driving force behind flow destabilization, as supported by its rapid augmentation in the downstream direction until approximately x = 0.28 m. A marginal increase in this term is also noted at the peak growth rate location for both injection scenarios.

Moreover, dissipation is predominantly influenced by the D_{HF} term, similar to scenarios where there is no blowing, and experiences intensified growth within the domain of transpiration gas introduction. The highest value is observed shortly before reaching the end of the injection location. While gas injection elevates production mechanisms mainly through increased P_{RS} and P_{En} , it concurrently heightens dissipation mechanisms, albeit not proportionally. As a result, overall flow destabilization ensues for the cases considered.

The substantial destabilization observed in the CO_2 case prompts an examination of its underlying causes. Our analysis indicates a significant influence of the dissipation term. Within the injection region, the CO_2 case exhibits comparable amplification to that of air owing to the total production term, as can be noted in Figure 11(f). Consequently, we attribute the heightened amplification in the CO_2 injection case to a notably lower contribution from the dissipation

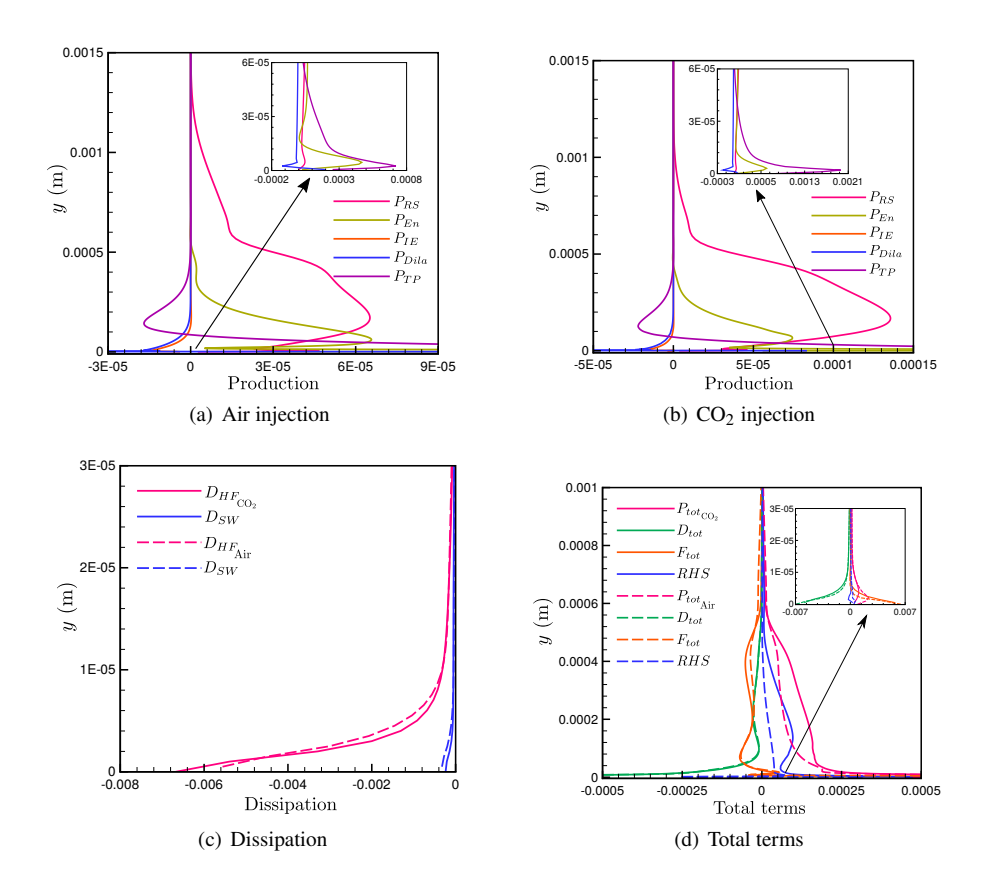


Fig. 12 Variation of dominant energy transfer terms plotted along the wall-normal direction at x = 0.2 m. The constituents of the production term for air and CO_2 injection are shown in (a) and (b), whereas dissipation and total energy transfer terms between both the cases are compared in (c) and (d), respectively, at 1200 kHz.

term. This trend is also mirrored in the flux terms, with their primary role in energy redistribution within the boundary layer, particularly at the boundaries.

To examine the active terms at various positions within the boundary layer, we plotted their variations for both air and CO_2 injection scenarios at the x=0.2 m in Figure 12. This specific location is denoted by a dashed line in the flow-field illustration shown in Figure 9 at 1200 kHz. The energy within the boundary layer is primarily generated by the Reynolds stress term P_{RS} , with the largest contribution near the wall coming from the P_{TP} term, followed by the entropy term P_{En} . In the context of CO_2 injection, the inset in Figure 12(b) shows that the production resulting from the entropy term is significantly less than the contributions from the variation in transport properties. However, for air injection, both P_{TP} and P_{En} are comparable near the wall. The dissipation terms exhibit a similar pattern within the boundary layer for both air and CO_2 , with their prominent presence observed in close proximity to the wall, as can be noticed in Figure 12(c). Finally, a summation of the production, dissipation, and flux terms, along with the total energy transfer terms, is illustrated in Figure 12(d). The insets in the figures indicate that the flux terms nearly offset the contribution from the dissipation term near the wall. Upon examining the total energy transfer term denoted as RHS, it is apparent that this term demonstrates a higher magnitude for CO_2 compared to air injection within the boundary layer. This results in a notably higher growth rate for CO_2 at x=0.2 m, as evidenced in Figure 8(b).

VI. Conclusions

The effect of transpiration cooling on the stability of a high-enthalpy boundary layer flow over a flat plate at Mach 4.35 was examined considering the injection of air and CO₂. In order to maintain a consistent mass-flux, air was injected at a higher velocity than CO₂ due to its lower density. The injection of CO₂ was observed to induce significant alterations in the transport and gas properties within the boundary layer. We noticed an approximately two-fold reduction

in the thermal diffusivity with CO_2 injection compared to the air injection scenario. Consequently, this resulted in a larger boundary layer thickness downstream of the injection location for the air case. Although there is a reduction in the thermal conductivity, the gradient in mean flow temperature increases when CO_2 is injected, which leads to a comparable variation in heat flux for both cases.

In comparison to the no-blowing case, both injection cases resulted in a substantial destabilization of the flow. The increased boundary layer thickness for the air case resulted in a shift in the neutral curve to lower frequencies. The unstable region was confined within the injection location for the air blowing case. Conversely, CO_2 injection resulted in a considerably larger unstable region, akin to the no-blowing scenario. Based on a transition N-factor of 9, it can be inferred that CO_2 injection will lead to an earlier transition to turbulence compared to air injection.

To investigate the observed differences in flow stability between air and CO_2 injection, an energy budget analysis was conducted. Before analyzing the various contributions from the disturbance energy balance equation, it was established that the additional terms resulting from considering Mack's norm for a spatial stability problem could be disregarded due to their small magnitude. Both production and dissipation terms showed an increase within the injection window. However, the key finding from the budget analysis was that the dissipation term was notably smaller for the CO_2 case as compared to air. Therefore, it can be concluded that the enhanced disturbance amplification in the CO_2 case primarily stemmed from the lower dissipation.

Acknowledgments

The authors extend their sincere gratitude for the financial support provided by the National Science Foundation under award number CBET-2146100, with Dr. R. Joslin serving as Program Manager. Furthermore, we appreciate the funding assistance from the Air Force Office of Scientific Research (AFOSR) under award number FA95502210464, with Dr. Amanda Chou serving as the program manager.

Appendix A

The following section provides further details on the employed governing equations, modelling the transport properties, and the evaluation of the chemical source term for fluid in thermo-chemical non-equilibrium. The total energy of a multi-component fluid is described by

$$E = \sum_{s}^{ns} \rho_s C_{v,tr,s} T + \sum_{s}^{ns} \rho_s e_{v,s} + \sum_{s}^{ns} \rho_s h_s^o + \frac{1}{2} \rho (u^2 + v^2 + w^2). \tag{9}$$

The translational and rotational specific heats at constant volume are assumed to be constant and given by

$$C_{v,t,s} = \frac{3}{2} \frac{R_u}{M_s} \tag{10}$$

and

$$C_{v,r,s} = \begin{cases} \frac{R_u}{M_s} & \text{for molecules,} \\ 0 & \text{for atoms and electrons.} \end{cases}$$
 (11)

where R_u is the universal gas constant and M_s is the molecular weight of species s. The total vibrational energy is then defined as

$$E_{\nu} = \sum_{s}^{ns} \rho_s e_{\nu,s} \tag{12}$$

with,

$$e_{v,s} = \begin{cases} \sum_{i=1}^{m} g_{s,i} \frac{R_u}{M_s} \frac{\theta_{v,s,i}}{\exp(\theta_{v,s,i}/T_{ve}) - 1} & \text{for molecules,} \\ 0 & \text{for atoms and electrons,} \end{cases}$$
(13)

where $\theta_{v,s,i}$ is the species characteristic vibrational temperature for species s and vibrational mode i, m denotes the number of vibrationally-activated energy modes for a given species, and $g_{s,i}$ denotes the degeneracy of the i-th energy

level of species s. Diatomic molecules can be modelled by a single vibrational energy level with a degeneracy of unity, while polyatomic species may have several vibrational energy levels. The specific heat at constant volume for the vibrational mode may then be given by

$$C_{v,v,s} = \frac{\partial e_{v,s}}{\partial T_v} = \begin{cases} \sum_{i=1}^m g_{s,i} \frac{R_u}{M_s} \frac{(\theta_{v,s,i}/T_v)^2 \exp(\theta_{v,s,i}/T_v)}{(\exp(\theta_{v,s,i}/T_v)-1)^2} & \text{for molecules,} \\ 0 & \text{for atoms and electrons.} \end{cases}$$
(14)

Appendix B outlines the various constants for modelling the vibrational and electronic effects.

The species viscosities and thermal conductivities are modelled using the Blottner (Eq. (15)) and Eucken (Eqs. (16) and (17)) relationships, respectively. In contrast, Wilke's model (Eqs. (18)-(20)) is used to compute the mixture properties [45]. The coefficients A_s , B_s , and C_s are presented in Table 2. The species conductivities can then be related to the species viscosity [46] where $C_{v,t,s}$, $C_{v,r,s}$, and $C_{v,v,s}$ are the specific heats at constant volume for the translational, rotational and vibrational energy modes using

$$\mu_s = 0.1 \exp\left[\left(A_s \ln(T) + B_s\right) \ln(T) + C_s\right],$$
(15)

$$\kappa_{tr,s} = \frac{5}{2} \mu_s C_{v,t,s} + \mu_s C_{v,r,s},\tag{16}$$

and

$$\kappa_{\nu,s} = \mu_s C_{\nu,\nu,s}. \tag{17}$$

Wilke's mixing rule is shown in Eqs. (18)-(20), where X_s is the molar fraction of species s,

$$\phi_{S} = \sum_{r}^{n_{S}} X_{r} \frac{\left[1 + \sqrt{\frac{\mu_{s}}{\mu_{r}}} \left(\frac{M_{r}}{M_{s}}\right)^{1/4}\right]^{2}}{\sqrt{8\left(1 + \frac{M_{s}}{M_{r}}\right)}},$$
(18)

$$\mu = \sum_{s}^{ns} \frac{X_s \mu_s}{\phi_s},\tag{19}$$

and

$$\kappa = \sum_{s}^{ns} \frac{X_s \kappa_s}{\phi_s}.$$
 (20)

The mass diffusion flux is assumed to follow Fick's first law as shown in Eq. (21) where ∇Y_s is the gradient of the species mass fraction, and D_s is the species diffusion coefficient. In this work, the species diffusion coefficients are approximated with a single binary coefficient D at a constant Lewis number, Le of 1.4, where $C_{p,\text{tr}}$ is the mixture translational/rotational specific heat at constant pressure.

$$I_s = -\rho D \nabla Y_s, \tag{21}$$

and

$$D = \frac{\text{Le}\kappa_{\text{tr}}}{\rho C_{p,\text{tr}}}.$$
 (22)

Sutton and Gnoffo (1998) [47] have noted that Fick's law does not guarantee that the mass diffusion fluxes will sum to zero, resulting in errors in capturing the correct mass fraction gradients, among other errors. Modified Fick's law is used in this work to improve the solution accuracy and is given by

$$J_{s\neq e} = I_s - Y_s \sum_{r\neq e}^{ns} I_r, \tag{23}$$

where *e* denotes the electron species (not included in this work) since the charge neutrality of the flow field must be handled separately. The viscous shear stresses are modelled based on a Newtonian fluid using Stokes' hypothesis.

$$\tau_{ij} = \mu \left(\frac{\partial u_j}{\partial x_i} + \frac{\partial u_i}{\partial x_j} \right) + \lambda \frac{\partial u_k}{\partial x_k} \delta_{ij}, \tag{24}$$

where,

$$\lambda = -\frac{2}{3}\mu,\tag{25}$$

and the heat fluxes are accounted for using Fourier's law as

$$q_{tr} = -\kappa_{tr} \nabla T \tag{26}$$

and

$$q_{v} = -\kappa_{v} \nabla T_{v}. \tag{27}$$

Finally, looking in more detail at the formulation of the chemical source term, the forward reaction rate is computed using an Arrhenius curve fit for the Park two-temperature model using the empirical coefficients given in Appendix C as,

$$k_{fr} = A_{fr} T_c^{\eta_r} \exp\left(-\frac{T_{ar}}{T_c}\right),\tag{28}$$

where,

$$T_c = T^{a_f} T_{ve}^{b_f}. (29)$$

Here, A_{fr} and η_r are coefficients for the Arrhenius curve fit, T_c is the forward controlling temperature, and T_{ar} represents the activation temperature. The values used for the Arrhenius curve fit can be found in Tables 4 and 5. The backward controlling reaction rate is a function of the forward reaction rate and the equilibrium constant, K_c , as computed using the backward controlling temperature, T_{bc} ,

$$k_{br}(T_{bc}) = \frac{k_{fr}(T_{bc})}{K_c(T_{bc})},$$
 (30)

where the backward controlling temperature is defined in Eq. (31) as

$$T_{bc} = T^{a_b} T^{b_b}_{ve}. (31)$$

For all dissociation reactions, the forward controlling temperature is computed using $a_f = 0.5$ and $b_f = 0.5$, whereas the backward dissociation reactions and all remaining exchange reactions are computed using $a_b=1$ and $b_b=0$. The equilibrium constant is computed using a NASA 9 polynomial curve fit for each species' normalized entropy and enthalpy, which may then be used to compute the normalized Gibb's free energy for each species [48]. The Gibb's free energy is defined as

$$\hat{g}_i = \hat{h}_i - T_{bc}\hat{s}_i,\tag{32}$$

where \hat{g}_i is the Gibbs energy per unit mole for species i, \hat{h}_i is the enthalpy per unit mole of species i, and \hat{s}_i is the entropy per unit mole for species i. The curve fits for the species enthalpy and entropy are given by

$$\frac{\hat{h}_i}{R_u T_{bc}} = -a_{1i} \frac{1}{T_{bc}^2} + a_{2i} \frac{\ln(T_{bc})}{T_{bc}} + a_{3i} + a_{4i} \frac{T_{bc}}{2} + a_{5i} \frac{T_{bc}^2}{3} + a_{6i} \frac{T_{bc}^3}{4} + a_{7i} \frac{T_{bc}^4}{5} + a_{9i} \frac{1}{T_{bc}}$$
(33)

and

$$\frac{\hat{s}_i}{R_u} = -a_{1i} \frac{1}{2T_{bc}^2} - a_{2i} \frac{1}{T_{bc}} + a_{3i} \ln(T_{bc}) + a_{4i} T_{bc} + a_{5i} \frac{T_{bc}^2}{2} + a_{6i} \frac{T_{bc}^3}{3} + a_{7i} \frac{T_{bc}^4}{4} + a_{10i}.$$
(34)

The equilibrium constant is a function of the change in the Gibbs free energy between the reactants and produces and is given by

$$K_c = \exp\left[-\sum_{i=1}^{ns} \left((v_{ir}^{"} - v_{ir}^{'}) \frac{\hat{g}_i}{R_u T_{bc}}\right)\right] \left(\frac{p_0}{R_u T_{bc}}\right)^{v_r}.$$
 (35)

The value of p_0 is a reference pressure set to 1 bar, while in the computational framework, p_0 is set to 0.1 and R_u is set to 8.31441 to be in the CGS unit system. The coefficients for the enthalpy and entropy curve fit are taken from the work of Gordon and McBride[49].

The translational-vibrational energy exchange source term, S_{t2v} , is based on the Landau-Teller formulation [46] given by

$$S_{t2v} = \sum_{s=mol.} \rho_s \frac{e_{v,s}(T) - e_{v,s}(T_v)}{\tau_s},$$
(36)

where $e_{v,s}(T)$ is the species vibrational energy at equilibrium, which is computed using the translational-rotational temperature, $e_{v,s}(T_v)$ is the species vibrational energy computed using the vibrational temperature, and τ_s is the relaxation time with the summation being taken over the molecular species only. The relaxation time is defined based on the molar averaged Landau-Teller relaxation time, $\langle \tau_s \rangle$ as

$$\tau_s = \langle \tau_s \rangle + \tau_{ps},\tag{37}$$

and τ_{ps} is Park's correction on the relaxation time for high-temperature effects beyond 8000 K [50]. The molar averaged relaxation time can be found with Eq. (38)

$$\left\langle \tau_s \right\rangle = \frac{\sum_r X_r}{\sum_r X_r / \tau_{sr}},\tag{38}$$

where τ_{sr} is the inter-species Landau-Teller relaxation time, which is modelled using a semi-empirical relation by Millikan and White for temperatures between 300 K and 8000 K as [51]

$$\tau_{sr} = \frac{p_0}{p} \exp\left[A_{sr} \left(T^{-1/3} - B_{sr}\right) - 18.42\right]. \tag{39}$$

The coefficients A_{sr} and B_{sr} are functions of the reduced molecular weight, μ_{sr} , and $\theta_{v,s}$ and defined as

$$A_{sr} = 0.0016 \mu_{sr}^{1/2} \theta_{v,s}^{4/3} \tag{40}$$

and

$$B_{sr} = 0.015 \mu_{sr}^{1/4} \tag{41}$$

where,

$$\mu_{sr} = \frac{M_s M_r}{M_s + M_r}. (42)$$

The characteristic vibrational temperature, $\theta_{v,s}$, used in the vibrational relaxation model corresponds to the first vibrationally activated energy level as it is assumed that the relaxation rate is dominated by the fastest energy level. The Park relaxation time correction is then defined based on the effective collision cross-section, σ_s , the average molecular velocity of species s, c_s , and the number density of the species, N_s , as

$$\tau_{ps} = \frac{1}{\sigma_s c_s N_s},\tag{43}$$

where,

$$\sigma_s = \sigma_s' \left(\frac{50000}{T}\right)^2 \quad \text{in m}^2 \tag{44}$$

and

$$c_s = \sqrt{\frac{8R_u T}{\pi M_s}}. (45)$$

In Eq. (44), σ'_s is an empirical factor used to correlate the numerical approximation to the experimental data [52]. Hence, this parameter would generally be species dependent; however, in this work, σ'_s is held fixed at 10^{-20} . The energy exchange into the vibrational energy mode due to chemical reactions is computed using the non-preferential model as

$$S_{c2v} = \sum_{s=mol.} \omega_s e_{v,s}.$$
 (46)

Appendix B: Species energy state and transport property data

Table 2 outlines the various species used in this work with their respective molecular weights, enthalpy of formation at 0 K (taken from Mutation++ [53]), and Blottner curve fit viscosity data [45].

Table 2 Basic species molecular and viscosity data.

Species	M_s (g/mol)	h_s^o (J/kg)	A_s	B_{s}	C_s
N_2	28	0.0000000E0	2.68142E-2	3.177838E-1	-1.13155513E1
O_2	32	0.0000000E0	4.49290E-2	-8.261580E-2	-9.20194750E0
NO	30	2.9961230E6	4.36378E-2	-3.355110E-2	-9.57674300E0
CO_2	44	-8.9425455E6	-1.95274E-2	1.047818E0	-1.43221200E1
CO	28	-3.9475000E6	-1.95274E-2	1.013295E0	-1.39787300E1
N	14	3.3621610E7	1.15572E-2	6.031679E-1	-1.24327495E1
O	16	1.5431190E7	2.03144E-2	4.294404E-1	-1.16031403E1
C	12	5.9723333E7	-1.00000E-4	7.928000E-1	-1.34154000E1

Table 3 gives the characteristic vibrational states of each species, with each diatomic molecule having a single vibrational energy state and polyatomic molecules such as CO₂ having three unique vibrational energy states.

Table 3 Species characteristic vibrational temperature for each vibrational mode.

Species	g_m	$\theta_{v}(K)$
N ₂	1	3395.0
O_2	1	2239.0
NO	1	2817.0
CO_2	2	960.2417
	1	1930.1809
	1	3379.9243
CO	1	3121.5194
N	1	0.0
O	1	0.0
C	1	0.0

Appendix C: Arrhenius Curve Fit Coefficients

Table 4 outlines all the dissociation reactions included in this work and the relevant parameters required to compute the forward reaction rates.

Table 4 Arrhenius curve fit coefficients for dissociation reactions.

	Reaction	Partner	T_c	A_{fr} (cm ³ /mol · s)	η_r	T_{ar} (K)	Source
1	$N_2 + M \rightleftharpoons N + N + M$	molecules	$\sqrt{TT_v}$	7.00E21	-1.60	1.132E5	Ref. 54
		atoms	$\sqrt{TT_v}$	3.00E22	-1.60	1.132E5	Ref. 54
2	$O_2 + M \rightleftharpoons O + O + M$	molecules	$\sqrt{TT_v}$	2.00E21	-1.50	5.936E4	Ref. 54
		atoms	$\sqrt{TT_v}$	1.00E22	-1.50	5.936E4	Ref. 54
3	$NO + M \rightleftharpoons N + O + M$	other	$\sqrt{TT_v}$	5.00E15	0.00	7.550E4	Ref. 55
		NO, CO_2, N, O, C	$\sqrt{TT_v}$	1.10E17	0.00	7.550E4	Ref. 55
4	$CO_2 + M \rightleftharpoons CO + O + M$	molecules	$\sqrt{TT_v}$	1.40E22	-1.50	6.3280E4	Ref. 56
		atoms	$\sqrt{TT_v}$	2.80E22	-1.50	6.3280E4	Ref. 56
_5	$CO + M \rightleftharpoons C + O + M$	all	$\sqrt{TT_v}$	3.00E21	-1.00	1.290E5	Ref. 56

Table 5 shows the exchange reactions used in this work with their respective forward reaction rate coefficients. All exchange reactions are evaluated at the same controlling temperature defined by the translational/rotational temperature.

Table 5 Arrhenius curve fit coefficients for exchange reactions.

	Reaction	T_c	A_{fr} (cm ³ /mol · s)	η_r	T_{ar} (K)	Source
6	$O_2 + N \rightleftharpoons NO + O$	T	2.49E9	1.18	4.010E3	Ref. 57
7	$N_2 + O \rightleftharpoons NO + N$	T	6.00E13	0.10	3.8000E4	Ref. 58
8	$CO + O \rightleftharpoons C + O_2$	T	3.90E13	-0.18	6.9200E4	Ref. 52
9	$CO_2 + O \rightleftharpoons O_2 + CO$	T	2.71E14	0.00	3.3800E4	Ref. 59
10	$CO + N \rightleftharpoons NO + C$	T	1.10E14	0.07	5.3500E4	Ref. 58
11	$CO + CO \rightleftharpoons CO_2 + C$	T	2.33E9	0.50	6.5710E4	Ref. 60
12	$CO + NO \rightleftharpoons CO_2 + N$	T	4.59E8	0.50	1.2070E4	Ref. 60
13	$N_2 + O_2 \rightleftharpoons NO + NO$	T	6.69E9	-2.54	6.4639E4	Ref. 61

Appendix D: Derivation of Energy Budget

The x-momentum (47), y-momentum (48), energy equation (49) and continuity equation (50) for the small amplitude disturbances are presented below.

$$\bar{\rho} \left(\frac{\partial \tilde{u}}{\partial t} + \bar{u} \frac{\partial \tilde{u}}{\partial x} + \tilde{u} \frac{\partial \bar{u}}{\partial x} + \bar{v} \frac{\partial \tilde{u}}{\partial y} + \tilde{v} \frac{\partial \bar{u}}{\partial y} \right) + \tilde{\rho} \left(\bar{u} \frac{\partial \bar{u}}{\partial x} + \bar{u} \frac{\partial \tilde{u}}{\partial x} + \bar{v} \frac{\partial \bar{u}}{\partial y} + \bar{v} \frac{\partial \tilde{u}}{\partial y} + \tilde{u} \frac{\partial \bar{u}}{\partial x} + \tilde{v} \frac{\partial \bar{u}}{\partial y} \right) \\
+ \frac{\partial \tilde{\rho}}{\partial x} - \bar{\mu} \left(2 \frac{\partial^2 \tilde{u}}{\partial x^2} + \frac{\partial^2 \tilde{u}}{\partial y^2} + \frac{\partial^2 \tilde{v}}{\partial x \partial y} \right) - \bar{\lambda} \left(\frac{\partial^2 \tilde{u}}{\partial x^2} + \frac{\partial^2 \tilde{v}}{\partial x \partial y} \right) - 2 \frac{d\bar{\mu}}{d\bar{T}} \left(\frac{\partial \tilde{u}}{\partial x} \frac{\partial \bar{T}}{\partial x} + \frac{\partial \tilde{T}}{\partial x} \frac{\partial \bar{u}}{\partial x} \right) \\
- 2 \frac{d\bar{\mu}}{d\bar{T}} \tilde{T} \left(2 \frac{\partial^2 \tilde{u}}{\partial x^2} + \frac{\partial^2 \tilde{u}}{\partial y^2} + \frac{\partial^2 \tilde{v}}{\partial x \partial y} \right) - \frac{d\bar{\mu}}{d\bar{T}} \left[\frac{\partial \bar{T}}{\partial y} \left(\frac{\partial \tilde{v}}{\partial x} + \frac{\partial \tilde{u}}{\partial y} \right) + \frac{\partial \tilde{T}}{\partial y} \left(\frac{\partial \bar{v}}{\partial x} + \frac{\partial \bar{u}}{\partial y} \right) \right] \\
- \frac{d\bar{\lambda}}{d\bar{T}} \left[\frac{\partial \bar{T}}{\partial x} \left(\frac{\partial \tilde{u}}{\partial x} + \frac{\partial \tilde{v}}{\partial y} \right) + \frac{\partial \tilde{T}}{\partial x} \left(\frac{\partial \bar{u}}{\partial x} + \frac{\partial \bar{v}}{\partial y} \right) + \tilde{T} \left(\frac{\partial^2 \bar{u}}{\partial x^2} + \frac{\partial^2 \bar{v}}{\partial x \partial y} \right) \right] \\
- \left[\left(\frac{\partial \bar{u}}{\partial y} + \frac{\partial \bar{v}}{\partial x} \right) \frac{\partial \bar{T}}{\partial y} + 2 \frac{\partial \bar{T}}{\partial x} \frac{\partial \bar{u}}{\partial x} \right] \frac{\partial^2 \bar{\mu}}{\partial \bar{T}^2} \tilde{T} - \left(\frac{\partial \bar{u}}{\partial x} + \frac{\partial \bar{v}}{\partial y} \right) \frac{\partial^2 \bar{\lambda}}{\partial \bar{T}^2} \frac{\partial \bar{T}}{\partial x} \tilde{T} = 0, \tag{47}$$

$$\bar{\rho} \left(\frac{\partial \tilde{v}}{\partial t} + \bar{u} \frac{\partial \tilde{v}}{\partial x} + \tilde{u} \frac{\partial \tilde{v}}{\partial x} + \bar{v} \frac{\partial \tilde{v}}{\partial y} + \tilde{v} \frac{\partial \tilde{v}}{\partial y} \right) + \bar{\rho} \left(\bar{u} \frac{\partial \bar{v}}{\partial x} + \bar{v} \frac{\partial \tilde{v}}{\partial y} \right) + \frac{\partial \tilde{p}}{\partial y} - \bar{\mu} \left(\frac{\partial^2 \tilde{v}}{\partial x^2} + 2 \frac{\partial^2 \tilde{v}}{\partial y^2} + \frac{\partial^2 \tilde{u}}{\partial x \partial y} \right) \\
- \bar{\lambda} \left(\frac{\partial^2 \tilde{v}}{\partial y^2} + \frac{\partial^2 \tilde{u}}{\partial x \partial y} \right) - \frac{d\bar{\mu}}{d\bar{T}} \left[\left(\frac{\partial \tilde{u}}{\partial y} + \frac{\partial \tilde{v}}{\partial x} \right) \frac{\partial \bar{T}}{\partial x} + \left(\frac{\partial \bar{u}}{\partial y} + \frac{\partial \bar{v}}{\partial x} \right) \frac{\partial \tilde{T}}{\partial x} + \tilde{T} \left(\frac{\partial^2 \tilde{v}}{\partial x^2} + 2 \frac{\partial^2 \tilde{v}}{\partial y^2} + \frac{\partial^2 \tilde{u}}{\partial x \partial y} \right) \right] \\
- 2 \frac{d\bar{\mu}}{d\bar{T}} \left(\frac{\partial \bar{T}}{\partial y} \frac{\partial \tilde{v}}{\partial y} + \frac{\partial \tilde{T}}{\partial y} \frac{\partial \tilde{v}}{\partial y} \right) - \frac{d\bar{\lambda}}{d\bar{T}} \left[\frac{\partial \bar{T}}{\partial y} \left(\frac{\partial \tilde{u}}{\partial x} + \frac{\partial \tilde{v}}{\partial y} \right) + \frac{\partial \tilde{T}}{\partial y} \left(\frac{\partial \tilde{u}}{\partial x} + \frac{\partial \tilde{v}}{\partial y} \right) + \tilde{T} \left(\frac{\partial^2 \bar{v}}{\partial y^2} + \frac{\partial^2 \tilde{u}}{\partial x \partial y} \right) \right] \\
- \left(\frac{\partial \bar{u}}{\partial x} + \frac{\partial \bar{v}}{\partial y} \right) \frac{\partial^2 \bar{\lambda}}{\partial \bar{T}^2} \frac{\partial \bar{T}}{\partial y} \tilde{T} - \left[\left(\frac{\partial \bar{u}}{\partial y} + \frac{\partial \bar{v}}{\partial x} \right) \frac{\partial \bar{T}}{\partial x} + 2 \frac{\partial \bar{T}}{\partial y} \frac{\partial \bar{v}}{\partial y} \right] \frac{\partial^2 \bar{\mu}}{\partial \bar{T}^2} \tilde{T} = 0, \tag{48}$$

$$\bar{\rho}C_{v}\left(\frac{\partial\tilde{T}}{\partial t} + \bar{u}\frac{\partial\tilde{T}}{\partial x} + u'\frac{\partial\bar{T}}{\partial x} + \bar{v}\frac{\partial\tilde{T}}{\partial y} + \tilde{v}\frac{\partial\bar{T}}{\partial y}\right) + \tilde{\rho}C_{v}\left(\bar{u}\frac{\partial\bar{T}}{\partial x} + \bar{v}\frac{\partial\bar{T}}{\partial y}\right) + \tilde{\rho}\left(\frac{\partial\bar{u}}{\partial x} + \frac{\partial\bar{v}}{\partial y}\right) + \bar{\rho}\left(\frac{\partial\bar{u}}{\partial x} + \frac{\partial\bar{v}}{\partial y}\right) + \frac{\partial\tilde{q}_{x}}{\partial x} + \frac{\partial\tilde{q}_{y}}{\partial y} - \bar{\tau}_{xx}\frac{\partial\bar{u}}{\partial x} - \tilde{\tau}_{xx}\frac{\partial\bar{u}}{\partial x} - \left(\frac{\partial\bar{u}}{\partial y} + \frac{\partial\bar{v}}{\partial x}\right)\tilde{\tau}_{xy} - \left(\frac{\partial\bar{u}}{\partial y} + \frac{\partial\bar{v}}{\partial x}\right)\tilde{\tau}_{xy} - \frac{\partial\bar{v}}{\partial y}\tilde{\tau}_{xy} - \bar{\tau}_{yy}\frac{\partial\bar{v}}{\partial y} - \tilde{\tau}_{yy}\frac{\partial\bar{v}}{\partial y} = 0,$$

$$\frac{\partial\tilde{\rho}}{\partial t} + \bar{\rho}\left(\frac{\partial\bar{u}}{\partial x} + \frac{\partial\bar{v}}{\partial y}\right) + \tilde{\rho}\left(\frac{\partial\bar{v}}{\partial y} + \frac{\partial\bar{u}}{\partial x}\right) + \bar{u}\frac{\partial\tilde{\rho}}{\partial x} + \bar{v}\frac{\partial\tilde{\rho}}{\partial y} + \tilde{u}\frac{\partial\bar{\rho}}{\partial x} + \tilde{v}\frac{\partial\bar{\rho}}{\partial y} = 0.$$
(50)

The heat flux and the components of the shear stress tensor can be expressed as

$$\begin{split} \tilde{q}_x &= -\bar{k}\frac{\partial \tilde{T}}{\partial x} - \tilde{k}\frac{\partial \bar{T}}{\partial x}, \quad \tilde{q}_y = -\bar{k}\frac{\partial \tilde{T}}{\partial y} - \tilde{k}\frac{\partial \bar{T}}{\partial y}, \\ \tilde{\tau}_{xx} &= (2\bar{\mu} + \bar{\lambda})\frac{\partial \tilde{u}}{\partial x} + \bar{\lambda}\frac{\partial \tilde{v}}{\partial y} + (2\tilde{\mu} + \tilde{\lambda})\frac{\partial \bar{u}}{\partial x} + \tilde{\lambda}\frac{\partial \bar{v}}{\partial y}, \\ \tilde{\tau}_{yy} &= (2\bar{\mu} + \bar{\lambda})\frac{\partial \tilde{v}}{\partial y} + \bar{\lambda}\frac{\partial \tilde{u}}{\partial x} + (2\tilde{\mu} + \tilde{\lambda})\frac{\partial \bar{v}}{\partial y} + \tilde{\lambda}\frac{\partial \bar{u}}{\partial x}, \\ \tilde{\tau}_{xy} &= \bar{\mu}\left(\frac{\partial \tilde{u}}{\partial y} + \frac{\partial \tilde{v}}{\partial x}\right) + \tilde{\mu}\left(\frac{\partial \bar{u}}{\partial y} + \frac{\partial \bar{v}}{\partial x}\right). \end{split}$$

To derive the total energy transfer equation, the disturbance continuity (50), x-momentum (47), y-momentum (48) and the energy equation (49) are multiplied by the coefficients of the Chu's energy norm, which are $R\bar{T}\tilde{\rho}/\bar{\rho}$, \tilde{u} , \tilde{v} and \tilde{T}/\bar{T} , respectively. The budget equation in terms of the total production P_{tot} , dissipation D_{tot} and the flux term F_{tot} can be written as

$$\frac{\partial \hat{E}}{\partial t} + \bar{\rho}\bar{u}\left(\hat{u}\frac{\partial \tilde{u}}{\partial x} + \hat{v}\frac{\partial \tilde{v}}{\partial x}\right) + \bar{\rho}\bar{v}\left(\hat{u}\frac{\partial \tilde{u}}{\partial y} + \hat{v}\frac{\partial \tilde{v}}{\partial y}\right) + \frac{\bar{P}\tilde{T}}{(\gamma - 1)\bar{T}^{2}}\left(\bar{u}\frac{\partial \tilde{T}}{\partial x} + \bar{v}\frac{\partial \tilde{T}}{\partial y}\right) \\
+ \frac{\bar{P}\tilde{\rho}}{\bar{\rho}^{2}}\left(\bar{u}\frac{\partial \tilde{\rho}}{\partial x} + \bar{v}\frac{\partial \tilde{\rho}}{\partial y}\right) = P_{\text{tot}} + D_{\text{tot}} + F_{\text{tot}},$$

$$\Rightarrow \frac{\partial \hat{E}}{\partial t} + P_{\text{Conv}} = P_{\text{tot}} + D_{\text{tot}} + F_{\text{tot}},$$

$$\Rightarrow \frac{D\hat{E}}{Dt} - \frac{(\hat{u}^{2} + \hat{v}^{2})}{2}\left(\bar{u}\frac{\partial \bar{\rho}}{\partial x} + \bar{v}\frac{\partial \bar{\rho}}{\partial y}\right) - \frac{R\hat{T}^{2}}{2(\gamma - 1)\bar{T}}\left[\bar{u}\left(\frac{\partial \bar{\rho}}{\partial x} - \frac{\bar{\rho}}{\bar{T}}\frac{\partial \bar{T}}{\partial x}\right) + \bar{v}\left(\frac{\partial \bar{\rho}}{\partial y} - \frac{\bar{\rho}}{\bar{T}}\frac{\partial \bar{T}}{\partial y}\right)\right] \\
- \frac{R\hat{\rho}^{2}}{2\bar{\rho}}\left[\bar{u}\left(\frac{\partial \bar{T}}{\partial x} - \frac{\bar{T}}{\bar{\rho}}\frac{\partial \bar{\rho}}{\partial x}\right) + \bar{v}\left(\frac{\partial \bar{T}}{\partial y} - \frac{\bar{T}}{\bar{\rho}}\frac{\partial \bar{\rho}}{\partial y}\right)\right] = P_{\text{tot}} + D_{\text{tot}} + F_{\text{tot}}.$$
(51)

Here,

$$\begin{split} \tilde{E} &= \frac{1}{2} \left(\frac{\bar{P}}{\bar{\rho}^2} \tilde{\rho} \tilde{\rho}^* + \bar{\rho} \tilde{u}_i \tilde{u}_i^* + \frac{\bar{P}}{(\gamma - 1)\bar{T}^2} \tilde{T} \tilde{T}^* \right), \\ P_{\text{Conv}} &= \bar{\rho} \bar{u} \left(\hat{u} \frac{\partial \tilde{u}}{\partial x} + \hat{v} \frac{\partial \tilde{v}}{\partial x} \right) + \bar{\rho} \bar{v} \left(\hat{u} \frac{\partial \tilde{u}}{\partial y} + \hat{v} \frac{\partial \tilde{v}}{\partial y} \right) \\ &+ \frac{\bar{P} \tilde{T}}{(\gamma - 1)\bar{T}^2} \left(\bar{u} \frac{\partial \tilde{T}}{\partial x} + \bar{v} \frac{\partial \tilde{T}}{\partial y} \right) + \frac{\bar{P} \tilde{\rho}}{\bar{\rho}^2} \left(\bar{u} \frac{\partial \tilde{\rho}}{\partial x} + \bar{v} \frac{\partial \tilde{\rho}}{\partial y} \right), \\ LHS_{extra} &= -\frac{(\hat{u}^2 + \hat{v}^2)}{2} \left(\bar{u} \frac{\partial \bar{\rho}}{\partial x} + \bar{v} \frac{\partial \bar{\rho}}{\partial y} \right) - \frac{R\hat{T}^2}{2(\gamma - 1)\bar{T}} \left[\bar{u} \left(\frac{\partial \bar{\rho}}{\partial x} - \frac{\bar{\rho}}{\bar{T}} \frac{\partial \bar{T}}{\partial x} \right) + \bar{v} \left(\frac{\partial \bar{\rho}}{\partial y} - \frac{\bar{\rho}}{\bar{T}} \frac{\partial \bar{T}}{\partial y} \right) \right] \\ &- \frac{R\hat{\rho}^2}{2\bar{\rho}} \left[\bar{u} \left(\frac{\partial \bar{T}}{\partial x} - \frac{\bar{T}}{\bar{\rho}} \frac{\partial \bar{\rho}}{\partial x} \right) + \bar{v} \left(\frac{\partial \bar{T}}{\partial y} - \frac{\bar{T}}{\bar{\rho}} \frac{\partial \bar{\rho}}{\partial y} \right) \right]; \end{split}$$

$$\begin{split} P_{tot} &= P_{RS} + P_{Mom} + P_{En} + P_{PW} + P_{Dila} + P_{IE} + P_{TP}, \\ D_{tot} &= D_{HF} + D_{SW}, \end{split}$$

 $F_{tot} = F_{TP} + F_{HF} + F_{PW} + F_{SW}.$

In addition,

$$\begin{split} \frac{D\hat{E}}{Dt} &= \frac{\partial \hat{E}}{\partial t} + \bar{u}\frac{\partial \hat{E}}{\partial x} + \bar{v}\frac{\partial \hat{E}}{\partial y}, \\ \frac{\partial \hat{E}}{\partial t} &= 0, \\ \bar{u}\frac{\partial \hat{E}}{\partial x} &= A + B, \\ A &= \frac{\bar{u}}{2}\left(\frac{\tilde{\rho}\tilde{\rho}^*}{\bar{\rho}^2}\frac{\partial \bar{P}}{\partial x} - \frac{\tilde{\rho}\tilde{\rho}^*\bar{P}}{\bar{\rho}^3}\frac{\partial \bar{\rho}}{\partial x} + \tilde{u}_i\tilde{u}_i^*\frac{\partial \bar{\rho}}{\partial x} + \frac{\tilde{T}\tilde{T}^*}{(\gamma - 1)\bar{T}^2}\frac{\partial \bar{P}}{\partial x} - \frac{\tilde{T}\tilde{T}^*\bar{P}}{(\gamma - 1)\bar{T}^3}\frac{\partial \bar{T}}{\partial x}\right), \\ B &= -2\alpha_i\bar{u}\hat{E}, \\ C &= \bar{v}\frac{\partial \hat{E}}{\partial y} &= \frac{\bar{v}}{2}\left(\frac{\tilde{\rho}\tilde{\rho}^*}{\bar{\rho}^2}\frac{\partial \bar{P}}{\partial y} - \frac{\tilde{\rho}\tilde{\rho}^*\bar{P}}{\bar{\rho}^3}\frac{\partial \bar{\rho}}{\partial y} + \tilde{u}_i\tilde{u}_i^*\frac{\partial \bar{\rho}}{\partial y} + \frac{\tilde{T}\tilde{T}^*}{(\gamma - 1)\bar{T}^2}\frac{\partial \bar{P}}{\partial y} - \frac{\tilde{T}\tilde{T}^*\bar{P}}{(\gamma - 1)\bar{T}^3}\frac{\partial \bar{T}}{\partial y}\right) \\ &+ \frac{\bar{v}}{2}\left[\frac{\bar{P}}{\bar{\rho}^2}(\tilde{\rho}\frac{\partial \tilde{\rho}^*}{\partial y} + \tilde{\rho}^*\frac{\partial \tilde{\rho}}{\partial y}) + \bar{\rho}(\tilde{u}_i\frac{\partial \tilde{u}_i^*}{\partial y} + \tilde{u}_i^*\frac{\partial \tilde{u}_i}{\partial y}) + \frac{\bar{P}}{(\gamma - 1)\bar{T}^2}(\tilde{T}\frac{\partial \tilde{T}^*}{\partial y} + \tilde{T}^*\frac{\partial \tilde{T}}{\partial y})\right]; \end{split}$$

$$LHS_{add} = A + B + C + LHS_{extra}$$

We have kept only the B term in the left hand side of Eq. (VI). The contribution of the additional term LHS_{add} is found to be negligible (see Figure). The components of each energy transfer mechanism are mentioned below.

$$\begin{split} & P_{RS} = - \, \bar{\rho} \left(\hat{u} \hat{u} \frac{\partial \bar{u}}{\partial x} + \hat{u} \hat{v} \frac{\partial \bar{u}}{\partial y} + \hat{u} \hat{v} \frac{\partial \bar{v}}{\partial x} + \hat{v} \hat{v} \frac{\partial \bar{v}}{\partial y} \right), \\ & P_{Mom} = - \left[\tilde{\rho} \tilde{u} \left(\bar{u} \frac{\partial \bar{u}}{\partial x} + \bar{v} \frac{\partial \bar{u}}{\partial y} \right) + \tilde{\rho} \tilde{v} \left(\bar{u} \frac{\partial \bar{v}}{\partial x} + \bar{v} \frac{\partial \bar{v}}{\partial y} \right) \right], \\ & P_{En} = - \left[\bar{\rho} R \left(\frac{\tilde{T}}{(\gamma - 1) \tilde{T}} - \frac{\tilde{\rho}}{\bar{\rho}} \right) \left(\tilde{u} \frac{\partial \bar{T}}{\partial x} + \tilde{v} \frac{\partial \bar{T}}{\partial y} \right) \right], \\ & P_{PW} = - \frac{\tilde{\rho}}{\bar{\rho}} \left(\tilde{u} \frac{\partial \bar{P}}{\partial x} + \tilde{v} \frac{\partial \bar{P}}{\partial y} \right), \\ & P_{IE} = - \frac{\tilde{\rho} C_{v} \tilde{T}}{\bar{T}} \left(\bar{u} \frac{\partial \bar{T}}{\partial x} + \bar{v} \frac{\partial \bar{T}}{\partial y} \right), \end{split}$$

$$\begin{split} \mathbf{P}_{\mathrm{TP}} = & \left[\left(2\bar{\mu} - \frac{\mathrm{d}\bar{\mu}}{\mathrm{d}\bar{T}} \bar{T} \right) \left[\frac{\partial \bar{v}}{\partial x} \left(\frac{\partial \bar{u}}{\partial y} + \frac{\partial \bar{v}}{\partial x} \right) + \frac{\partial \bar{u}}{\partial y} \left(\frac{\partial \bar{u}}{\partial y} + \frac{\partial \bar{v}}{\partial x} \right) + 2 \frac{\partial \bar{u}}{\partial x} \frac{\partial \bar{u}}{\partial x} + 2 \frac{\partial \bar{v}}{\partial y} \frac{\partial \bar{v}}{\partial y} \right] \\ & + \left(2\bar{\lambda} - \frac{\mathrm{d}\bar{\lambda}}{\mathrm{d}\bar{T}} \bar{T} \right) \left(\frac{\partial \bar{v}}{\partial y} + \frac{\partial \bar{u}}{\partial x} \right) \left(\frac{\partial \bar{u}}{\partial x} + \frac{\partial \bar{v}}{\partial y} \right) \\ & + \frac{\mathrm{d}\bar{\mu}}{\mathrm{d}\bar{T}} \bar{T} \left[2 \left(\frac{\partial \bar{u}}{\partial x} \right)^2 + 2 \left(\frac{\partial \bar{v}}{\partial y} \right)^2 + \left(\frac{\partial \bar{v}}{\partial x} \right)^2 + \left(\frac{\partial \bar{u}}{\partial y} \right)^2 + 2 \frac{\partial \bar{u}}{\partial y} \frac{\partial \bar{v}}{\partial x} \right] \\ & + \frac{\mathrm{d}\bar{\lambda}}{\mathrm{d}\bar{T}} \bar{T} \left[\left(\frac{\partial \bar{u}}{\partial x} \right)^2 + \left(\frac{\partial \bar{v}}{\partial y} \right)^2 + 2 \frac{\partial \bar{u}}{\partial x} \frac{\partial \bar{v}}{\partial y} \right] + \frac{\bar{k}}{\bar{T}} \left(\frac{\partial \bar{T}}{\partial x} \frac{\partial \bar{T}}{\partial x} + \frac{\partial \bar{T}}{\partial y} \frac{\partial \bar{T}}{\partial y} \right) \\ & + \left[\frac{\partial}{\partial x} \left(\bar{T} \frac{\mathrm{d}\bar{k}}{\mathrm{d}\bar{T}} \frac{\partial \bar{T}}{\partial x} \right) + \frac{\partial}{\partial y} \left(\bar{T} \frac{\mathrm{d}\bar{k}}{\mathrm{d}\bar{T}} \frac{\partial \bar{T}}{\partial y} \right) \right] \right] \bar{T}, \\ \mathbf{P}_{\mathrm{Dila}} = & - \left(\frac{\tilde{P}\bar{T}}{\bar{T}} + \frac{\tilde{P}\bar{P}^2}{\bar{P}^2} \right) \left(\frac{\partial \bar{u}}{\partial x} + \frac{\partial \bar{v}}{\partial y} \right), \\ \mathbf{D}_{\mathrm{SW}} = & - \left[\bar{\tau}_{xx_1} \frac{\partial \bar{u}}{\partial x} + \bar{\tau}_{yy_1} \frac{\partial \bar{v}}{\partial y} + \bar{\tau}_{xy_1} \left(\frac{\partial \bar{v}}{\partial x} + \frac{\partial \bar{u}}{\partial y} \right) \right], \\ \mathbf{P}_{\mathrm{TP}} = & 2 \frac{\partial}{\partial x} \left(\bar{\mu} \bar{u} \frac{\partial \bar{u}}{\partial x} \right) + \frac{\partial}{\partial x} \left(\bar{\lambda} \bar{u} \frac{\partial \bar{u}}{\partial x} \right) + \frac{\partial}{\partial x} \left(\bar{u} \bar{v} \frac{\partial \bar{v}}{\partial y} \right) + \frac{\partial}{\partial y} \left(\bar{\mu} \bar{u} \frac{\partial \bar{u}}{\partial y} \right) + \frac{\partial}{\partial x} \left(\bar{\mu} \bar{v} \frac{\partial \bar{u}}{\partial y} \right) \\ & + \frac{\partial}{\partial x} \left(\bar{\lambda} \bar{u} \frac{\partial \bar{v}}{\partial x} \right) + \frac{\partial}{\partial y} \left(\bar{\lambda} \bar{u} \frac{\partial \bar{u}}{\partial x} \right) + \frac{\partial}{\partial y} \left(\bar{\mu} \bar{v} \frac{\partial \bar{v}}{\partial y} \right) + \frac{\partial}{\partial y} \left(\bar{\mu} \bar{u} \frac{\partial \bar{u}}{\partial y} \right) + \frac{\partial}{\partial y} \left(\bar{\mu} \bar{u} \frac{\partial \bar{u}}{\partial y} \right) + \frac{\partial}{\partial y} \left(\bar{\mu} \bar{u} \frac{\partial \bar{u}}{\partial y} \right) \right], \\ \mathbf{F}_{\mathrm{PW}} = & - \left[\frac{\partial}{\partial x} \left(\bar{u} \tilde{u} \tilde{v} \right) + \frac{\partial}{\partial y} \left(\bar{v} \tilde{v} \tilde{v}_{y_1} \right) + \frac{\partial}{\partial y} \left(\bar{v} \tilde{v}_{y_{11}} \right) + \frac{\partial}{\partial y} \left(\bar{v} \tilde{v}_{y_{11}} \right) + \frac{\partial}{\partial y} \left(\bar{v} \tilde{v}_{y_{21}} \right) + \frac{\partial}{\partial y} \left(\bar{v} \tilde{v}_{x_{21}} \right) + \frac{\partial}{\partial y} \left(\bar{u} \tilde{v} \tilde{v}_{x_{21}} \right) \right], \\ \mathbf{F}_{\mathrm{SW}} = & \frac{\partial}{\partial x} \left(\bar{u} \tilde{u} \tilde{v}_{x_{21}} \right) + \frac{\partial}{\partial y} \left(\bar{v} \tilde{v}_{y_{21}} \right) + \frac{\partial}{\partial y} \left(\bar{v} \tilde{v}_{x$$

The heat flux and stress tensor can be written as,

$$\begin{split} \tilde{q}_{x_1} &= -\bar{k} \frac{\partial \tilde{T}}{\partial x}, \quad \tilde{q}_{y_1} &= -\bar{k} \frac{\partial \tilde{T}}{\partial y}, \\ \tilde{\tau}_{xx_1} &= (2\bar{\mu} + \bar{\lambda}) \frac{\partial \tilde{u}}{\partial x} + \bar{\lambda} \frac{\partial \tilde{v}}{\partial y}, \\ \tilde{\tau}_{yy_1} &= (2\bar{\mu} + \bar{\lambda}) \frac{\partial \tilde{v}}{\partial y} + \bar{\lambda} \frac{\partial \tilde{u}}{\partial x}, \\ \tilde{\tau}_{xy_1} &= \bar{\mu} \left(\frac{\partial \tilde{u}}{\partial y} + \frac{\partial \tilde{v}}{\partial x} \right). \end{split}$$

Appendix E

A grid convergence study was conducted to ensure that the results were independent of the grid. In Figure 13, the heat flux distribution along the wall is depicted, indicating that there is negligible variation in heat transfer rates for wall-normal spacing beyond $dy_w = 10^{-6}$ m. Therefore, a grid with $dy_w = 10^{-6}$ m was chosen for all the simulations performed in this study.

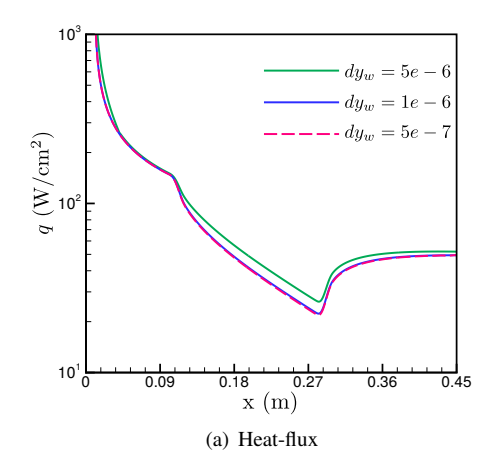


Fig. 13 The effect of varying wall-normal spacing on the heat-flux plotted along the wall for the air injection case with a velocity of 0.3 m/s.

References

- [1] Hermann, T., McGilvray, M., and Naved, I., "Performance of transpiration-cooled heat shields for reentry vehicles," *AIAA Journal*, Vol. 58, No. 2, 2020, pp. 830–841.
- [2] Holden, M., Wadhams, T., and Mundy, E., "A review of experimental studies of surface roughness and blowing on the heat transfer and skin friction to nosetips and slender cones in high mach numbers flows," 40th Thermophysics Conference, 2008, p. 3907.
- [3] Kuhn, M., Hald, H., Gülhan, A., Esser, B., and Olivier, H., "Experimental Investigations of Transpiration Cooled CMC's in Supersonic Plasma Flows," *Thermal Protection Systems and Hot Structures*, Vol. 631, 2006.
- [4] Esser, B., Gülhan, A., and Kuhn, M., "Thermal qualification of transpiration cooling for atmospheric entry," *Proceedings of the 1st CEAS European Air and Space Conference*, 2007, pp. 3205–3210.
- [5] Esser, B., and Gülhan, A., "Qualification of active cooling concepts in ground facilities," RESPACE–Key Technologies for Reusable Space Systems, Springer, 2008, pp. 104–131.
- [6] Gülhan, A., and Braun, S., "An experimental study on the efficiency of transpiration cooling in laminar and turbulent hypersonic flows," *Experiments in fluids*, Vol. 50, No. 3, 2011, pp. 509–525.
- [7] Liu, Y.-Q., Jiang, P.-X., Jin, S.-S., and Sun, J.-G., "Transpiration cooling of a nose cone by various foreign gases," *International journal of heat and mass transfer*, Vol. 53, No. 23-24, 2010, pp. 5364–5372.
- [8] van Foreest, A., Sippel, M., Gülhan, A., Esser, B., Ambrosius, B., and Sudmeijer, K., "Transpiration cooling using liquid water," *Journal of Thermophysics and Heat Transfer*, Vol. 23, No. 4, 2009, pp. 693–702.
- [9] Wang, J., Zhao, L., Wang, X., Ma, J., and Lin, J., "An experimental investigation on transpiration cooling of wedge shaped nose cone with liquid coolant," *International Journal of Heat and Mass Transfer*, Vol. 75, 2014, pp. 442–449.
- [10] Shen, L., Wang, J., Dong, W., Pu, J., Peng, J., Qu, D., and Chen, L., "An experimental investigation on transpiration cooling with phase change under supersonic condition," *Applied Thermal Engineering*, Vol. 105, 2016, pp. 549–556.

- [11] Luan, Y., He, F., Wang, J., Wu, Y., and Zhu, G., "An experimental investigation on instability of transpiration cooling with phase change," *International Journal of Thermal Sciences*, Vol. 156, 2020, p. 106498.
- [12] Pappas, C. C., and Okuno, A. F., "Measurements of Skin Friction of the Compressible Turbulent Boundary Layer on a Cone with Foreign Gas Injection," *Journal of the Aerospace Sciences*, Vol. 27, No. 5, 1960, pp. 321–333. https://doi.org/10.2514/8.8533.
- [13] Marvin, J. G., and Akin, C. M., "Combined effects of mass addition and nose bluntness on boundary-layer transition," *AIAA Journal*, Vol. 8, No. 5, 1970, pp. 857–863. https://doi.org/10.2514/3.5778.
- [14] Schneider, S. P., "Hypersonic boundary-layer transition with ablation and blowing," *Journal of Spacecraft and Rockets*, Vol. 47, No. 2, 2010, pp. 225–237.
- [15] Jewell, J., Leyva, I., Parziale, N. J., and Shepherd, J. E., "Effect of gas injection on transition in hypervelocity boundary layers," 28th International Symposium on Shock Waves, Springer, 2012, pp. 735–740.
- [16] Schmidt, B. E., and Shepherd, J. E., "Stability of Supersonic Flow with Injection," AIAA Journal, Vol. 57, No. 12, 2019, pp. 5230–5240. https://doi.org/10.2514/1.J058080.
- [17] Johnson, H., Gronvall, J., and Candler, G., "Reacting Hypersonic Boundary Layer Stability with Blowing and Suction," 2009. https://doi.org/10.2514/6.2009-938.
- [18] Ghaffari, S., Marxen, O., Iaccarino, G., and Shaqfeh, E., "Numerical Simulations of Hypersonic Boundary-Layer Instability with Wall Blowing," 2010. https://doi.org/10.2514/6.2010-706.
- [19] Mortensen, C. H., and Zhong, X., "Real-Gas and Surface-Ablation Effects on Hypersonic Boundary-Layer Instability over a Blunt Cone," *AIAA Journal*, Vol. 54, No. 3, 2016, pp. 980–998. https://doi.org/10.2514/1.J054404.
- [20] Li, F., Choudhari, M., Chang, C.-L., and White, J., "Effects of injection on the instability of boundary layers over hypersonic configurations," *Physics of Fluids*, Vol. 25, No. 10, 2013, p. 104107.
- [21] Saikia, B., and Brehm, C., "Effects of Injection Gas Composition on the Stability of a High-Enthalpy Flow over a Blunt Cone," 2024. https://doi.org/10.2514/6.2024-1977.
- [22] Miró Miró, F., and Pinna, F., "Injection-gas-composition effects on hypersonic boundary-layer transition," *Journal of Fluid Mechanics*, Vol. 890, 2020, p. R4. https://doi.org/10.1017/jfm.2020.129.
- [23] Leyva, I., Laurence, S., Beierholm, A., Hornung, H., Wagnild, R., and Candler, G., "Transition delay in hypervelocity boundary layers by means of CO2/acoustic instability interactions," 47th AIAA Aerospace Sciences Meeting Including the New Horizons Forum and Aerospace Exposition, 2009, p. 1287.
- [24] Wagnild, R., Candler, G., Leyva, I., Jewell, J., and Hornung, H., "Carbon dioxide injection for hypervelocity boundary layer stability," 48th AIAA Aerospace Sciences Meeting Including the New Horizons Forum and Aerospace Exposition, 2010, p. 1244.
- [25] Fedorov, A. V., Soudakov, V., and Leyva, I. A., "Stability analysis of high-speed boundary-layer flow with gas injection," 2014. https://doi.org/10.2514/6.2014-2498.
- [26] Saikia, B., Al Hasnine, S., and Brehm, C., "On the role of discrete and continuous modes in a cooled high-speed boundary layer flow," *Journal of Fluid Mechanics*, Vol. 942, 2022, p. R7. https://doi.org/https://doi.org/10.1017/jfm.2022.380.
- [27] Park, C., "Assessment of Two-Temperature Kinetic Model for Ionizing Air," *Journal of Thermophysics and Heat Transfer*, Vol. 3, 1989, pp. 233–244. https://doi.org/10.2514/3.28771.
- [28] Wilke, C., "A viscosity equation for gas mixtures," The Journal of Chemical Physics, Vol. 18, No. 4, 1950, pp. 517–519.
- [29] Blottner, F. G., Johnson, M., and Ellis, M., "Chemically reacting viscous flow program for multi-component gas mixtures," Tech. rep., Sandia Labs., Albuquerque, N. Mex., 1971.
- [30] Eucken, A., "Uber die Temperaturabhangigkeit der Warmeleitfahigkeit einiger Gase," Phys. Z, Vol. 14, No. 8, 1913, pp. 324–332.
- [31] Zibitsker, A. L., McQuaid, J. A., Stern, E. C., Palmer, G. E., Libben, B., Brehm, C., and Martin, A., "Finite-rate and equilibrium study of graphite ablation under arc-jet conditions," *Computers & Fluids*, 2023. https://doi.org/10.1016/j.compfluid.2023.106069.
- [32] McQuaid, J. A., and Brehm, C., "Heat flux predictions for hypersonic flows with an overset near body solver on an adaptive block-structured Cartesian off-body grid," *Computers & Fluids*, Vol. 269, 2024, p. 106121. https://doi.org/https://doi.org/10.1016/j.compfluid.2023.106121.

- [33] McQuaid, J. A., Zibitsker, A. L., Martin, A., and Brehm, C., "Simulation of Graphite Ablation using an Overset Near Body Solver on an Adaptive Block-Structured Cartesian Off-Body Grid," AIAA Aviation Forum, American Institute of Aeronautics and Astronautics, 2022. https://doi.org/10.2514/6.2022-4088.
- [34] Brehm, C., Barad, M. F., Housman, J. A., and Kiris, C. C., "A comparison of higher-order finite-difference shock capturing schemes," *Computers & Fluids*, Vol. 122, 2015, pp. 184–208. https://doi.org/10.1016/j.compfluid.2015.08.023.
- [35] Brehm, C., "On Consistent Boundary Closures for Compact Finite-Difference WENO schemes," *Journal of Computational Physics*, Vol. 334, 2017, pp. 573–581. https://doi.org/10.1016/j.jcp.2016.12.057.
- [36] Haas, A. P., Browne, O. M., Fasel, H. F., and Brehm, C., "A Numerical Jacobian Based Linearized Compressible Navier-Stokes Solver For Hypersonic Boundary-Layer Stability," 47th AIAA Fluid Dynamics Conference, 2017, p. 4520. https://doi.org/https://doi.org/10.2514/6.2017-4520.
- [37] Haas, A. P., Browne, O. M., Fasel, H. F., and Brehm, C., "A time-spectral approximate Jacobian based linearized compressible Navier-Stokes solver for high-speed boundary-layer receptivity and stability," *Journal of Computational Physics*, Vol. 405, 2020, p. 108978. https://doi.org/https://doi.org/10.1016/j.jcp.2019.108978.
- [38] Balay, S., Gropp, W. D., McInnes, L. C., and Smith, B. F., "Efficient management of parallelism in object-oriented numerical software libraries," *Modern software tools for scientific computing*, Springer, 1997, pp. 163–202.
- [39] Amestoy, P. R., Duff, I. S., and L'Excellent, J.-Y., "MUMPS multifrontal massively parallel solver version 2.0," 1998.
- [40] Miró Miró, F., and Pinna, F., "Effect of uneven wall blowing on hypersonic boundary-layer stability and transition," *Physics of Fluids*, Vol. 30, No. 8, 2018, p. 084106. https://doi.org/10.1063/1.5043353, URL https://doi.org/10.1063/1.5043353.
- [41] Fedorov, A., and Tumin, A., "High-speed boundary-layer instability: old terminology and a new framework," *AIAA journal*, Vol. 49, No. 8, 2011, pp. 1647–1657.
- [42] Chu, B.-T., "On the energy transfer to small disturbances in fluid flow (Part I)," Acta Mechanica, Vol. 1, No. 3, 1965, pp. 215–234.
- [43] Mack, L. M., Boundary-layer stability theory, Jet Propulsion Laboratory, 1969.
- [44] Al Hasnine, S., Russo, V., Tumin, A., and Brehm, C., "Biorthogonal decomposition of the disturbance flow field generated by particle impingement on a hypersonic boundary layer," *Journal of Fluid Mechanics*, Vol. 969, 2023, p. A1. https://doi.org/https://doi.org/10.1017/jfm.2023.531.
- [45] Blottner, F. G., Johnson, M., and Ellis, M., "Chemically Reacting Viscous Flow Program for Multi-Component Gas Mixtures," Tech. Rep. SC-RR-70-754, Sandia Laboratories, January 1971.
- [46] Vincenti, W. G., and Kruger, C. H., *Equilibrium Gas Properties*, 1st ed., Krieger Publishing Company, 1975, Chaps. 5, 6, pp. 152–196.
- [47] Sutton, K., and Gnoffo, P. A., "Multi-Component Diffusion with Application to Computational Aerothermodynamics," 7th AIAA/ASME Joint Thermophysics and Heat Transfer Conference, AIAA, 1998. https://doi.org/10.2514/6.1998-2575.
- [48] Gordon, S., and McBride, B. J., "Computer Program for Calculation of Complex Chemical Equilibrium Compositions and Applications, Part I: Analysis," Tech. Rep. NASA-RP-1311, NASA Lewis Research Center, October 1994.
- [49] McBride, B. J., Heimel, S., Ehlers, J. G., and Gordon, S., "Thermodynamic Properties to 6000K for 210 Substances Involving the First 18 Elements," Tech. Rep. NASA-SP-3001, NASA Lewis Research Center, January 1963.
- [50] Park, C., Nonequilibrium Hypersonic Aerothermodynamics, 1st ed., Wiley-Interscience, Moffet Field, California, 1990.
- [51] Millikan, R. C., and White, D. R., "Systematics of Vibrational Relaxation," *Journal of Chemical Physics*, Vol. 39, 1963, pp. 3209–3213. https://doi.org/10.1063/1.1734182.
- [52] Park, C., Howe, J. T., and Jaffe, R. L., "Review of Chemical-Kinetic Problems of Future NASA Missions, II: Mars Entries," Journal of Thermophysics and Heat Transfer, Vol. 8, 1994, pp. 9–23. https://doi.org/10.2514/3.496.
- [53] Scoggins, J. B., Leroy, V., Bellas-Chatzigeorgis, G., Dias, B., and Magin, T. E., "Mutation++: MUlticomponent Thermodynamic And Transport properties for IONized gases in C++," *SoftwareX*, Vol. 12, 2020. https://doi.org/10.1016/j.softx.2020.100575.

- [54] Park, C., Jaffe, R. L., and Partridge, H., "Chemical-Kinetic Parameters of Hyperbolic Earth Entry," *Journal of Thermophysics and Heat Transfer*, Vol. 15, 2001, pp. 76–90. https://doi.org/10.2514/2.6582.
- [55] Park, C., Howe, J. T., and Jaffe, R. L., "Chemical-Kinetic Problems of Future NASA Missions," 29th Aerospace Sciences Meeting, 1991. https://doi.org/10.2514/6.1991-464.
- [56] Johnston, C. O., Brandis, A. M., and Sutton, K., "Shock Layer Radiation Modeling and Uncertainty for Mars Entry," 43rd AIAA Thermophysics Conference, American Institute of Aeronautics and Astronautics, 2012. https://doi.org/10.2514/6.2012-2866.
- [57] Bose, D., and Candler, G. V., "Thermal Rate Constants of the O₂ + N → NO + O Reaction based on the A2' and A4' Potential-Energy Surfaces," *The Journal of Chemical Physics*, Vol. 107, 1997, pp. 6136–6145. https://doi.org/10.1063/1.475132.
- [58] Fujita, K., Yamada, T., and Ishii, N., "Impacts of Ablation Gas Kinetics on Hyperbolic Earth Entry Radiative Heating," *44th AIAA Aerospace Sciences Meeting and Exhibit*, American Institute of Aeronautics and Astronautics, 2006. https://doi.org/10.2514/6.2006-1185.
- [59] Ibragimova, L. B., "Recommended Rate Constants of CO + O₂ Reversible CO₂ + O Reactions," *Khim. Fiz.*, Vol. 10, 1991, pp. 307–310.
- [60] Mitcheltree, R. A., and Gnoffo, P. A., "Wake Flow about a MESUR Mars Entry Vehicle," 6th AIAA/ASME Joint Thermophysics and Heat Transfer Conference, AIAA, 1994. https://doi.org/10.2514/6.1994-1958.
- [61] Mortensen, C., "Effects of Thermochemical Nonequilibrium on Hypersonic Boundary-Layer Instability in the Presence of Surface Ablation or Isolated Two-Dimensional Roughness," Ph.D. thesis, University of California, Los Angeles, Los Angeles, California, 2015.